CLASSIFICATION: PHYSICAL SCIENCES, chemistry, physics

Determination and Evaluation of the Non-Additivity in Wetting of Molecularly Heterogeneous Surfaces

Zhi Luo,[1]† Anna Murello,[1]† David M. Wilkins,[1]† Filip Kovacik,[2] Joachim Kohlbrecher,[3] Aurel Radulescu,[4] Halil I. Okur,[2] Quy K. Ong,[1] Sylvie Roke,[1,2] Michele Ceriotti,[1] Francesco Stellacci[1,2]*

[1]Institute of Materials, École Polytechnique Fédérale de Lausanne, 1015 Lausanne, Switzerland.
[2]Institute of Bioengineering, École Polytechnique Fédérale de Lausanne, 1015 Lausanne, Switzerland.
[3]Laboratory for Neutron Scattering and Imaging, Paul-Scherrer Institut, 5232 Villigen, Switzerland.
[4]Forschungszentrum Jülich Gmbh, Jülich Center for Neutron Science, JCNS at Heinz Maier-Leibnitz Zentrum, Lichtenbergstraße 1, 85747 Garching, Germany.

†These authors contributed equally to this work.

*Corresponding author: Francesco Stellacci
EPFL STI IMX SUNMIL
MXG 030 (Bâtiment MXG)
Station 12
CH-1015 Lausanne
+41 21 69 37872
francesco.stellacci@epfl.ch

Abstract

The interface between water and folded proteins is very complex. Proteins have 'patchy' solvent accessible areas composed of domains of varying hydrophobicity. The textbook understanding is that these domains contribute additively to interfacial properties (Cassie's equation, CE). An ever-growing number of modelling papers question the validity of CE at molecular length scales, but there is no conclusive experiment to support this and no proposed new theoretical framework. Here, we study the wetting of model compounds with patchy surfaces differing solely in patchiness but not in composition. Were CE to be correct, these materials would have had the same work of adhesion (W_{SL}) and time averaged structure of interfacial water. We find considerable differences in W_{SL} and sum frequency generation measurements of the water structure show distinctively different spectral features. Molecular dynamics simulations of water on patchy surfaces capture the observed behaviors and point towards significant non-additivity in water density and average orientation. They show that a description of the molecular arrangement on the surface is needed to predict its wetting properties. We propose a predictive model that considers, for every molecule, the contributions of its first nearest neighbors as a descriptor to determine the wetting properties of the surface. The model is validated by measurements of W_{SL} in multiple solvents, where large differences are observed for solvents whose effective diameter is smaller than ~6Å. The experiments and theoretical model proposed here should represent a departure point for the study of complex biological interfaces as well as for the engineering of synthetic ones.

Keywords: hydration, hydrophobic, wetting, nanostructured

Significance statement:

Every folded protein presents an interface with water that is composed of domains of varying hydro-philicity/-phobicity. Many simulations studies have highlighted the non-additivity in the wetting of such nanostructured surfaces in contrast with the accepted theoretical formula that is additive. We present here an experimental study on surfaces of identical composition but different organization of hydrophobic and hydrophilic domains. We prove that the interfacial energy of such surfaces differs by ~20% and that a significant difference in the interfacial water H-bonding structure can be measured. As a result, in combination with molecular dynamics simulations, we

propose a model that captures the wetting of molecularly heterogeneous surface, showing the importance of local structure (first nearest neighbors) in determining the wetting properties.

Text

It is well-established that a large number of protein properties derive from their solvent accessible surface(1). It is also known that such surfaces are highly structured with patches of varying composition and hydrophobicity. Such complexity affects a number of interfacial properties ranging from the work of adhesion (W_{SL}, the main component in the interfacial energy(2)) to the very complex time averaged structure of interfacial water (TASIW)(3). Whether these properties (as well as many others such as hydrophobic forces) are additive or not is a matter of intense debate(4–7). Classical thermodynamics for multicomponent interfaces treats W_{SL} additively. For example, one rigorous formulation for Cassie's equation (CE) in the case of a perfectly flat surface with two components A and B, is the following

$$W_{SL} = f_A W_A + f_B W_B \qquad (1)$$

Several computational studies have appeared recently suggesting strong effects of patchiness on the density of interfacial water (typically used in simulation as a proxy for W_{SL}) that cannot be explained in the framework of Eq. 1(7–11). To the best of our knowledge, there is no direct experimental evidence supporting these claims. Some of us have used indirect observations (i.e. non-monotonic dependence of W_{SL} on surface composition) to substantiate the existence of a geometrical effect in W_{SL}(12). Recently, experimental evidences of related physical phenomena have been published; Abbott and co-workers showed structural and chemical effects on hydrophobic forces(13), while Aida and co-workers showed local effects on ion pairing(14). No direct experimental support for the rapidly growing computational work(7, 9–11, 15) has yet been presented and no experimental or theoretical study has proposed a theoretical framework to capture all of the results.

In the experimental cases discussed above, self-assembled monolayers (SAMs) composed of a mixture of hydrophobic and hydrophilic molecules were used as model surfaces. None of these studies could investigate one of the true key components of these interfaces, the time averaged structure of interfacial water (TASIW). This is unfortunate, as it is the TASIW that is studied in

all simulations. Unfortunately, probing the effect of patchiness on TASIW is a significant challenge when model systems (as well as proteins) differ both in composition and geometrical parameters, as it is impossible to decouple effects due to one or the other. Hence, there is no experimental evidence on the role of patchiness on TASIW. Here, to tackle this question, we have developed model compounds, i.e. gold nanoparticles coated with SAMs composed of a binary mixture of hydrophobic and hydrophilic ligands that separate into patches(16, 17). These model nanoparticles were produced in two forms differing solely in the geometrical parameters of the patches, but not in composition or any other structural parameters.

We used nanoparticles coated with a 1:1 binary mixture of perdeuterated 3-mercaptopropionic acid (dMPA) and 1-octanethiol (OT). These nanoparticles were chosen as they form patchy ligand shells, due to the fact that MPA is hydrophilic and OT hydrophobic, and that the longer OT gains conformational entropy at the edges of the patches. Also, they were expected to have non-additive W_{SL} as they have been shown to have non-monotonic solubility in various solvents(18). Similar nanoparticles have shown patches in their ligand shell that at room temperature did not change for days, but could be evolved into smaller patches by gentle heating(19). We started by exchanging, at room temperature, MPA ligands onto the ligand shell of OT nanoparticles. The exchange was tuned to lead to a 1:1 ligand shell composition(19). The ligand shell composition was determined by nuclear magnetic resonance (NMR) studies after etching the gold core. The resulting nanoparticles were then heated at 70°C for 4 h, in order to bring the ligand shell morphology to a different state. All the detailed synthesis and characterization procedures are described in Supplementary Discussion.

After thermal treatment, care was taken to prove that no changes had occurred to the nanoparticles and that only the ligand shell morphology had changed. Small angle X-ray scattering (SAXS) was performed on the nanoparticles. As shown in Figure 1A, the SAXS curves for the nanoparticles before and after thermal treatment overlap to an impressive degree. SAXS probes almost exclusively the nature (size and polydispersity) of the gold cores of the nanoparticles, as contrast in X-ray scales with the atomic number. The overlap between the two curves indicates that the gold cores were not affected by the thermal treatment either in size or in polydispersity. This is particularly important to guarantee that the curvature of the surface is the same for the two sets of

nanoparticles. We then focused on characterizing the ligand shell before and after thermal treatment. Some of the characterizations were performed on nanoparticles coated with MPA and OT (as opposed to d-MPA and OT). This choice was imposed by the technique used, in the case of ^{1}H NMR because of its incompatibility with deuterated molecules, while in the case of thermogravimetric analysis (TGA) because of the large amount of sample required. We assume that these particles are identical to the deuterated ones. They were all obtained by place exchange reactions that started from the same OT nanoparticles and we have previously shown that deuteration of ligands does not change the properties of the nanoparticles(20, 21). A complete discussion on this topic can be found in the Supplementary Discussion. As is common in nanoparticle characterization(22), the ligand shell composition was determined by etching the gold cores after having made sure that no free ligand was in solution (i.e. no sharp peak in the NMR of the whole nanoparticles, Figure S2). Figure 1B compares the two NMR spectra achieved in this way. No measurable difference in the relative integration of the peaks was found, indicating no change in the ligand shell composition (in both cases the ligand ratio was found to be approximately MPA: OT = 55%: 45%). We performed TGA to determine ligand density on the nanoparticles. Figure 1C shows that the two TGA curves are well within instrumental error of each other (the difference in the plateau is < 2 % in mass and the accepted instrumental error is >5%). This indicated that the ligand shell density did not change. Given that the relative ratio of the ligands and the total density did not change, we can conclude that the average number of OT and of MPA molecules on the nanoparticles before and after thermal treatment are the same. Finally, infrared spectroscopy (Figure 1D) measurements show that the protonation state of the carboxylic acid had not changed, as both spectra show only a peak at 1600 cm^{-1} corresponding to the asymmetric stretching of deprotonated carboxylic group. Hence, we can conclude that the chemical composition of the ligand shell did not change upon thermal treatment. In Table S1 we report a summary of all the results of the characterization performed on these particles.

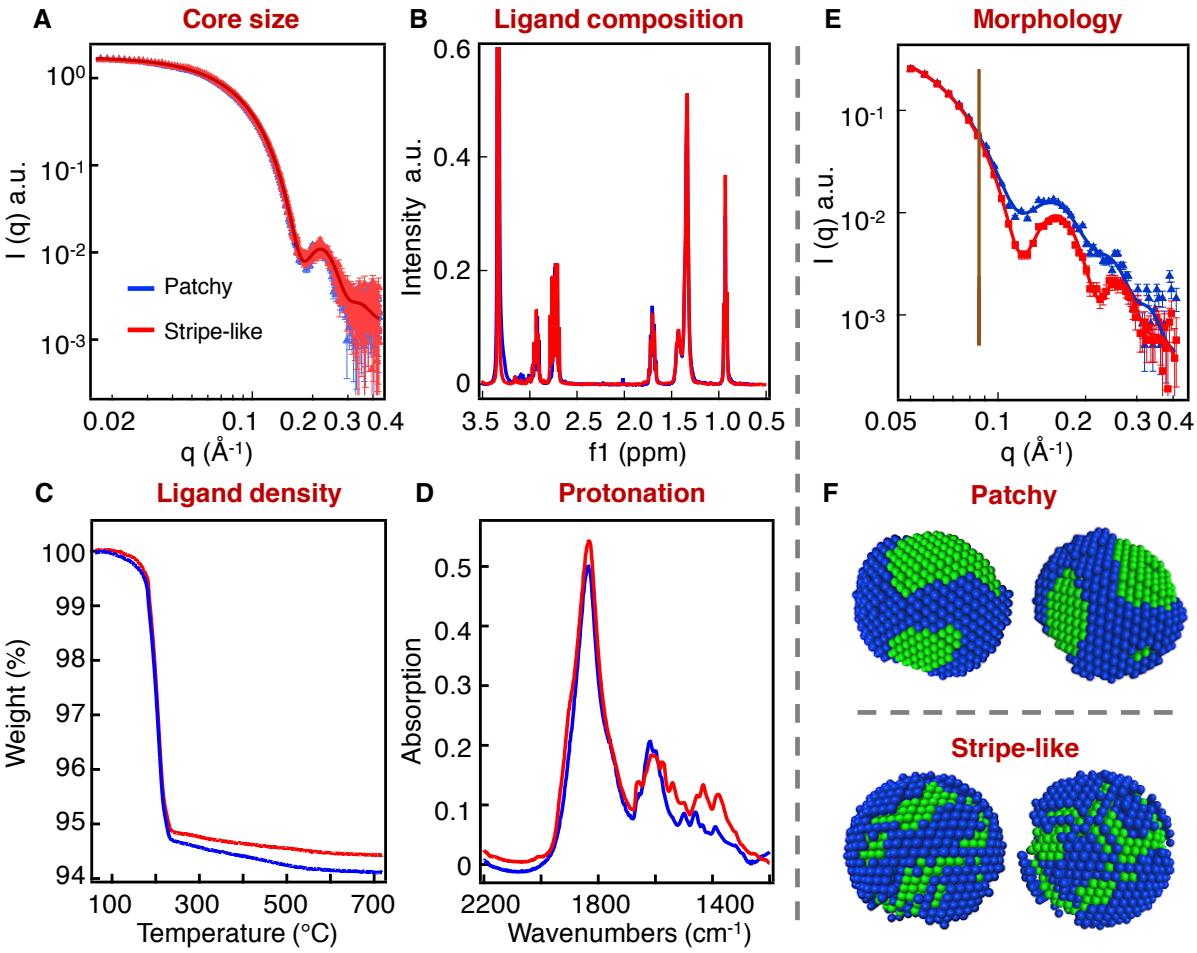

Figure 1. Characterization of the nanoparticles with OT and per-deuterated MPA used in this paper. In all plots the blue and red lines refer to nanoparticles before and after thermal treatment respectively. Note for all measurements but SANS the curves practically overlap. (A) SAXS data on both nanoparticles were measured using ethanol as solvent. A fit with a Gaussian distribution gives a core size of 4.9 ± 0.6 nm, consistent with TEM data shown in Figure S1. (B) NMR spectra of the ligands detached from their core via an iodine decomposition(23). The measured ligand ratio is approximately MPA: OT = 55%: 45%. NMR spectra before decomposition are shown in Figure S2 (C) TGA plots for both particles showing that the ligand density is unaffected by the thermal treatment. Note that in TGA the experimental error is considered to be larger than 5%. (D) FTIR measurements taken from nanoparticle film in ATR mode. The spectra show that MPA ligands are mainly deprotonated on both nanoparticles. (E) SANS spectra of nanoparticles taken in tetrahydrofuran-d8. The overlap in the low q region (below 0.083 $Å^{-1}$ corresponding to the overall size of the NP in real space, as indicated by the vertical line) shows that the two nanoparticles have

the same radius of gyration. The scattering curves at higher q range are the only characterization that shows a significant difference for the two nanoparticles, indicating a difference in the shape of nanoparticles (i.e. patchiness of the ligand shell). (F) Low-resolution models for the nanoparticles obtained by fitting the curves shown in (D) and in chloroform-d (dots are the experimental measures, and lines are the fits) using a method described recently(21). Detailed fitting procedures are described in Supplementary Discussion. In the SANS model, the blue beads stand for OT ligands while the green ones are MPA ligands. We should point out that the Nanoparticles characterized in (B) and (C) are nanoparticles coated with OT and MPA instead of dMPA. These nanoparticles are identical to the ones described in the other panels as discussed in Supplementary Discussion.

In striking contrast to what is described above, small angle neutron scattering (SANS) led to significantly different scattering curves for the two nanoparticles (Figure 1E), i.e. there are substantial differences in the scattering form factors of the nanoparticles. Indeed, the SANS of the thermally treated nanoparticles shows more pronounced oscillations, indicating a shape that is more centrosymmetric when compared to the untreated nanoparticles. Such changes in form factors, given all the other measurements described above, can be assigned solely to differences in the overall shape of the nanoparticles. Given that the gold core had no change in form factor (as derived from SAXS), this means that the form factor change in SANS has to be attributed to a change in the shape of the ligand shell. The latter was proven not to change in chemical nature, so that the only remaining possibility is a change in the patchiness. Such effects of thermal treatment on the morphology of nanoparticles are reproduced at two different neutron scattering facilities, as shown in Figure S3, which confirms that the differences in the scattering profile are not due to instrumentation. Using a method recently reported(21), we were able to determine the morphology of the patches using SANS curves recorded with different solvent contrast and *ab initio* calculations. A detailed description can be found in the Supplementary Discussion and all the SANS spectra utilized with their fitting are shown in Figure S4. The resulting models for the ligand shells show a patchy type morphology for nanoparticles before thermal treatment and stripe-like structure after thermal treatment, as presented in Figure 1F. By quantifying the characteristic length-scales of the patches from the SANS modeling(21), we find that the average MPA domain

thickness is 2.1 ± 0.6 nm and 1.3 ± 0.3 nm for the patchy (untreated) and stripe-like (thermally treated) nanoparticles respectively.

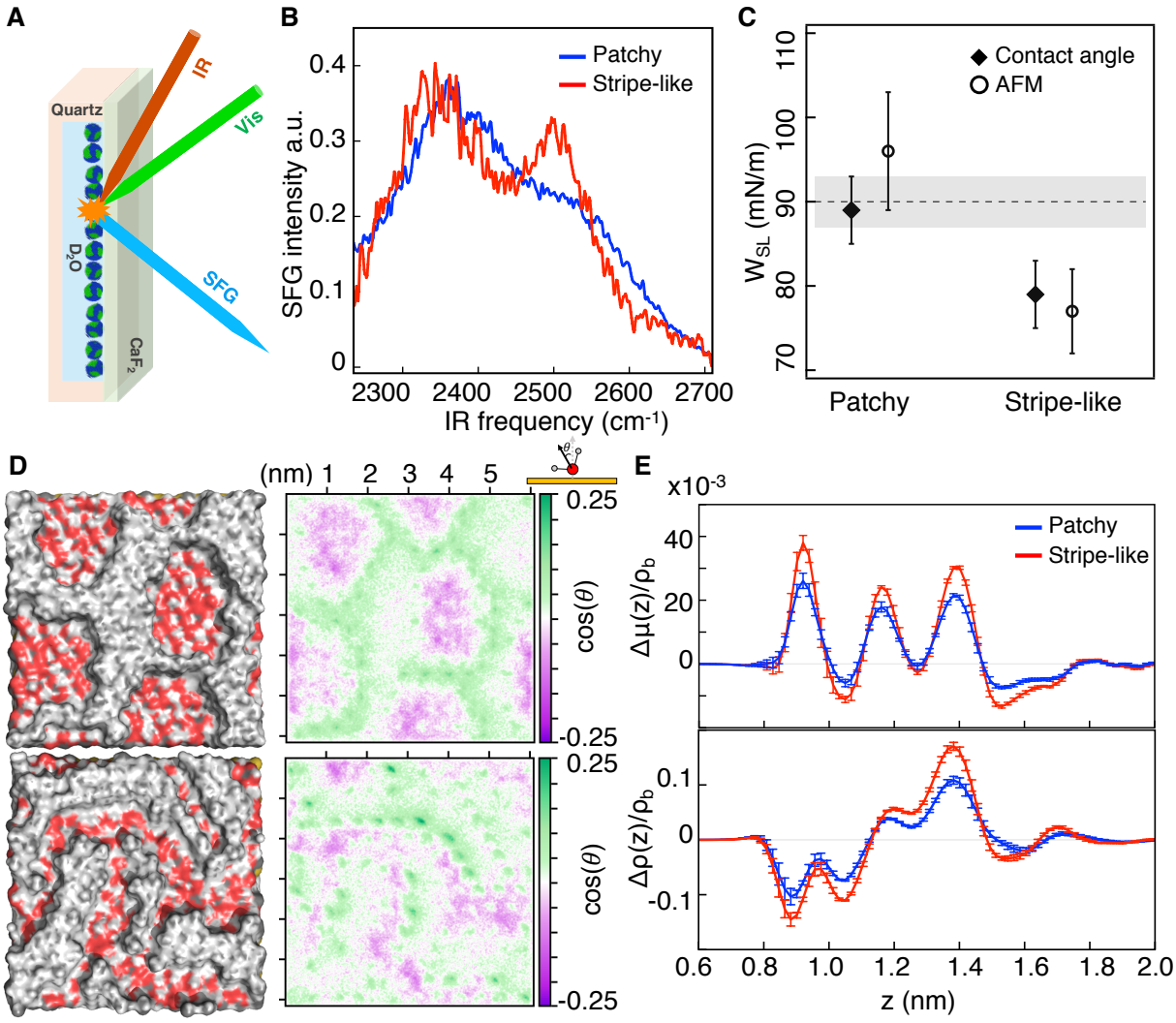

Figure 2. Experimental characterization and molecular dynamics simulations of the water interfaces around the nanoparticles. (A) Schematic of the SFG setup. The SSP polarization is used to measure the interfacial hydrogen bond strength. (B) SFG spectra collected at the nanoparticle-water interface. The D-bond network has significantly higher fraction of weak bonds for stripe-like nanoparticles. (C) Measurements of the W_{SL} for films of nanoparticles, obtained independently using two techniques, contact angle (black diamonds) and AFM (white circles). The measurements show large differences. The dotted line represents the additive averages for the W_{SL} of the two homoligand nanoparticles measured using contact angle. The gray band is the error in

the measurements. (D) Left: morphology of the surfaces in the simulation, after equilibration. Water molecules have been removed to show the geometry of the interface. Carbon, oxygen and hydrogen atoms are represented with grey, red and white colors respectively. Right: corresponding 2D histogram of the average dipole orientation density, μ, above the surfaces (averaged over four different realizations). Areas on top of the MPA patches look mostly purple (dipole pointing towards the surface) and areas on top of the OT patches look mostly white (dipole parallel to the surface). Green regions (dipole pointing out from the surface) are visible on top of the OT-MPA interfaces, with darker green visible on the stripe-like morphology. (E) Deviation from the additive assumption of the average dipole orientation density, Δμ, (top) and density profile of water, Δρ (bottom), as a function of the distance from the gold surface (z).

Given that the shape of the nanoparticles and the chemical nature and composition of their ligand shell was the same, we were able to characterize the TASIW for both particles, as any difference found would be due solely to the different geometrical structure of the ligand shell. We used vibrational sum frequency generation (SFG) to characterize the interfacial water structure as it is a surface sensitive technique that has been proven to effectively characterize the vibrational spectra of interfacial water(24). Figure 2A presents an illustration of an SFG experiment. Films of nanoparticles were produced on CaF_2 surfaces by drop casting ethanol nanoparticles solutions. Detailed procedures and parameters are described in Supplementary Discussion. We first used SFG to characterize the C-H stretching peaks of the OT ligands in the two nanoparticles. As described in the Supplementary Discussion and Figure S5, the SFG spectra for these stretching modes for the two nanoparticles agree with the SANS models. Figure 2B shows the interfacial water structure as measured in the O-D stretch region of the SFG spectrum, the spectra were found to differ considerably. The spectra have two main features, i.e. a peak at ~2375 cm^{-1} and a peak at ~2530 cm^{-1}, corresponding to interfacial water that have stronger (2375 cm^{-1}) and weaker hydrogen bonds. It can be seen from Figure 2B that the TASIW is different for the two nanoparticles. Water molecules at the interfaces with the two nanoparticles experience different intermolecular H-bond environments. In the case of water at the interface with the patchy nanoparticle, the 2530 cm^{-1} band is mostly a shoulder of the 2375 cm^{-1} band. For the case of the stripe-like nanoparticle, the 2530 cm^{-1} band has almost the same intensity as the 2375 cm^{-1} band. To make sure that these effects were not due to film morphology but due to wetting at the single nanoparticle level, multiple

spectra were recorded on different films, the spectra are shown in Figure S6. The general conclusion is that in the case of stripe-like structure the ratio of the 2530 cm^{-1} band to the 2375 cm^{-1} band is larger than that for the patchy nanoparticle. An over-simplified interpretation of these data is that water molecules are less structured near the stripe-like nanoparticles than near the patchy nanoparticles.

We then went on to establish whether such differences would lead to different W_{SL}. We first measured contact angles for films of the two nanoparticles and derived the W_{SL}, as listed in Table S2. In Figure 2C we show that the W_{SL} for the patchy nanoparticles is close to the average of the W_{SL} of the two homoligand nanoparticles, while a deviation is found for the nanoparticles with stripe-like morphology. To further confirm these data, we employed a recently developed technique(25) based on small amplitude modulation atomic force microscopy (AFM) to measure the W_{SL} (additional information can be found in Supplementary Discussion and Figure S7). Also in this case we found a difference between the two samples (Figure 2C). It should be stressed that this latter technique is based on different working principles than contact angle measurements, and measures W_{SL} at the single nanoparticle level, removing completely the effect of roughness on the measurement. The agreement between the two measurements strongly validates the conclusions. Averaging the results from the two independent techniques we can conclude that the difference between the W_{SL} on the two nanoparticles is 15 ± 7 mN/m (~17% of the expected additive value), the stripe-like nanoparticles being more hydrophobic. Additional results on a different set of nanoparticles are reported in Table S3.

The experimental evidence we have provided thus far shows that the hydrophobicity of the nanoparticles depends on the morphology of the SAM in a non-additive way, and that the effect is connected to the TASIW. In order to capture the relationship between surface morphology and TASIW structure, we performed large-scale molecular dynamics (MD) simulations of a forcefield model of SAMs composed of mixtures of OT and MPA (in its protonated form) together with water. We generated two configurations (Figure 2D) that are consistent with the ligand distributions seen on the patchy and stripe-like surfaces. It is found that water on top of the patchy and stripe-like configurations exhibits a complex behavior, i.e. realistic arrangements of ligands do not lend themselves to a simple interpretation in terms of clear-cut molecular motifs. In Figure

2D we show the time averaged dipole orientation density of the water molecules at the interfaces. It is obvious that the two surfaces lead to different angular distributions. We notice that the water dipoles point towards the surface on top of the MPA patches and lie parallel to the surface on top of the OT patches. The dipoles point out from the surface at the interface between OT and MPA. We find a larger number of dipoles pointing out from the surface on the stripe-like morphology because of the MPA-OT interfaces are closer to each other. The integrated dipole orientation density μ together with the water density profile ρ for the two SAM geometries are then calculated to illustrate the SAM-induced water ordering. The theoretical μ and ρ profiles based on an additive assumption are also calculated by simulating pure OT and MPA SAM surfaces. The deviations of μ and ρ from the additive assumption are then plotted as a function of the position on the surface (Figure 2E). One can see that the dipole and density profiles above both SAMs do not follow a purely additive behavior and that there are significant differences between the two morphologies. Data resulting from the simulation of two additional surface are reported on Figure S8 and show the high reproducibility of the obtained results.

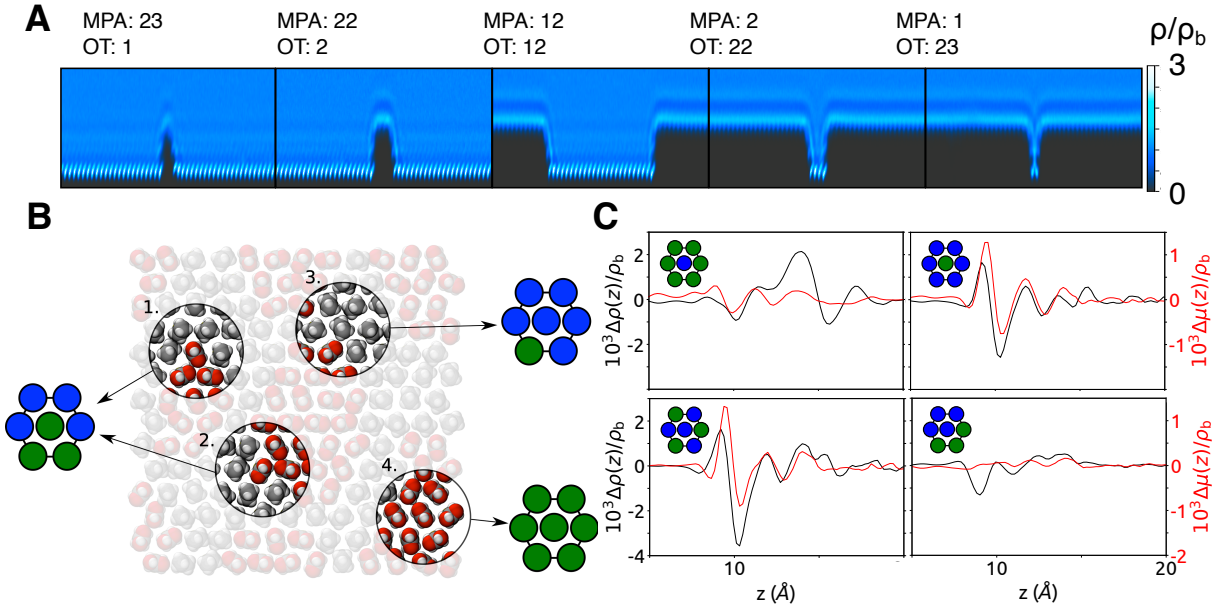

Figure 3. Water density on heterogeneous surfaces. (A) Water density in a cut across trenches of varying size. Ligands occupy the black area of the pictures (shorter ligands are MPA, longer ligands are OT). (B) Schematics of the nearest-neighbor classification scheme showing four ligands with their surrounding environments: patterns 1 and 2 are equivalent by rotational symmetry, with an MPA ligand at the center, surrounded by two other MPA ligands in an "ortho"

configuration; pattern 3 has an OT ligand at the center with five other OT ligands surrounding it; pattern 4 has an MPA ligand surrounded by five other MPA ligands, and does not contribute to the excess term. (C) Example of surface excesses associated with some of the possible nearest neighbor configurations.

In order to propose a quantitative model for these non-additive effects, we began by performing molecular dynamics simulations of a series of "trench" configurations corresponding to rectangular OT and MPA regions of varying width (Figure S9), where we expect that the boundary between the two types of ligand is responsible for non-additive behavior as in Eq. 1. Figure 3A shows the structuring of water in a cut across trenches of varying sizes, where it can clearly be seen that the pattern of the water density at the boundaries of the trenches is very similar for all trenches that are more than one molecule thick; for these narrower trenches clear differences are observed (a detailed description of the results can be found in the Supplementary Discussion and in Figures S10 and S11). Specifically, the water density on a single MPA molecule, surrounded by OT, is smaller than the one on MPA thicker trenches. On the contrary, the water density on a single OT molecule, surrounded by MPA, is higher than the one on OT thicker trenches. Overall these observations suggest that the water density on a ligand is affected primarily by its first nearest neighbors.

This led us to rethink Eq. 1. The non-additivity in the systems containing trenches is due to the water structure at the boundary between two types of ligand. However, these systems contain only straight boundaries between ligands of different types, and do not provide an exhaustive list of possible nearest-neighbors configurations, limiting the power of a model based on trench systems to predict the results of a general surface. For this reason, we then generated a set of simulation boxes in which the ligands in each site on both the top and the bottom surfaces were chosen randomly. Assuming that the contribution of a particular ligand to non-additivity depends only on the identities of its first nearest neighbors, and treating the long-range structure as a mean field, each ligand on a surface was classified according to the identities and dispositions of its first nearest neighbors. Figure 3B illustrates the definition of a particular ligand's environment, and the supplementary discussion and Figure S12 describe the classification of these ligands. Using the excess terms $\Delta\mu$ and $\Delta\rho$ for these randomly generated surfaces, we built a linear regression model, in which an excess quantity for an arbitrary surface is predicted as,

$$\Delta f(z) = \sum n_i f_i(z) \qquad (2)$$

where f = μ or ρ, n_i is the number of ligands of type i, and $f_i(z)$ is a function to be fitted. This is analogous to the cluster expansion models that are used e.g. to describe the thermodynamic properties of multi-component alloys (26, 27). Here, we use this approximation to model excess terms associated with a particular distribution of ligands. Figure 3C shows the excess terms associated with some of the possible nearest neighbors arrangements (the full set of possibilities is shown in Figure S12). These examples have been chosen to show two effects. The first of these is asymmetry between the two ligand types: the excess term associated with a single MPA molecule surrounded by six OT molecules is significantly different from that associated with one OT molecule surrounded by six MPA molecules. The second is that the excess terms are not determined only by the number of nearest neighbors of a certain kind but also on their arrangement (with "patchy" patterns usually being associated with smaller excesses).

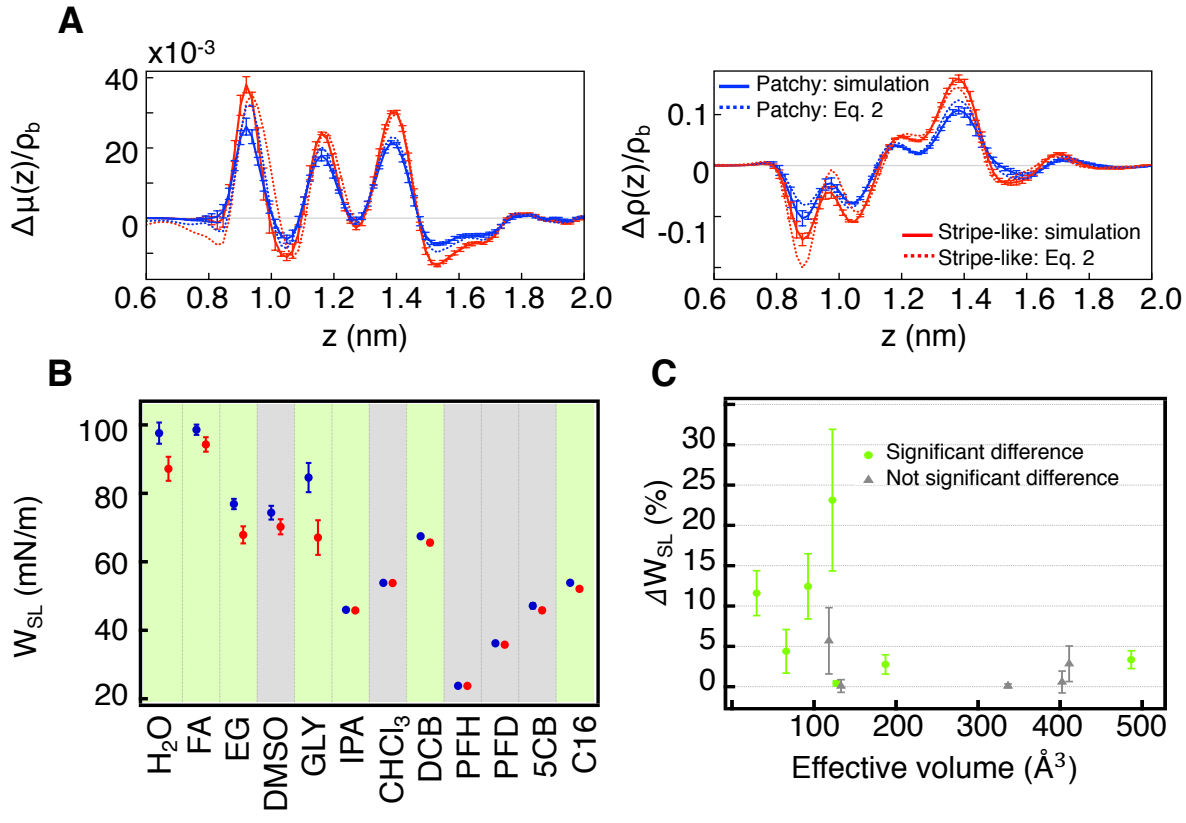

Figure 4. Model capturing the non-additivity of interface-dependent properties. (A) Surface excess Δρ and Δμ of the patchy and stripe-like surfaces as calculated from MD simulations and calculated

by the linear regression model. (B) W_{SL} values of the patchy (blue) and stripe-like (red) nanoparticles in various solvents. The green shadings indicate solvents in which the W_{SL} shows significant differences (Student's t-Test assuming equal variances, p = 0.05) for the two nanoparticles. The grey shadings indicate that the null hypothesis ("the two nanoparticles have the same work of adhesion") cannot be rejected. (The solvents used are the following: water (H_2O), formamide (FA), ethylene glycol (EG), dimethyl sulfoxide (DMSO), glycerol (GLY), isopropanol (IPA), chloroform ($CHCl_3$), dichlorobenzene (DCB), perfluorohexane (PFH), perfluorodecalin (PFD), 4-Cyano-4'-n-pentylbiphenyl (5CB), hexadecane (C16). (C) Dependence of the differences of W_{SL} (ΔW_{SL}) of the two films on the effective volume of the solvent molecules. The color of the points is the same as the one of the shadings in (3) and relates to the significance of the differences in W_{SL}.

Figure 4A shows the predictions of this model for the surface excesses of the patchy and striped systems. The excellent match between the excess values resulting from the simulations (continuous lines) with the ones resulting from the predictions derived from Eq. 2 (dotted lines) indicates that the first nearest neighbors are sufficient to determine the excess term associated with a single molecule in the SAM. Therefore, we expect the work of adhesion between the SAM and a solvent not to be affected by the surface heterogeneity when the solvent molecules are larger then the intermolecular distance in the SAM (because a single solvent molecule will interact with more than one molecule on the surface at any time). To test this prediction, we measured W_{SL} in films of the nanoparticles described above for a series of solvents. Every time a new film was produced, its contact angle with water was measured, to make sure the roughness was homogeneous. All the contact angle data as well as the solvent properties are listed in Table S4. As shown in Figure 4B, some solvents have the same W_{SL} for the patchy and stripe-like nanoparticles, while others behave as water, featuring different W_{SL}. To rationalize these results along the lines of Eq. 2, we calculated the effective molecular volume (V_{eff}) of all the solvents by dividing their molecular weight by the product of the solvent density and the Avogadro number. We plotted the differences in W_{SL} (ΔW_{SL}) against V_{eff} and the results were striking (Figure 4C). Solvents whose V_{eff} is above ~125 $Å^3$ (corresponding to an effective diameter of ~ 6 Å, comparable with the intermolecular distance on the SAM: ~ 5 Å) show a ΔW_{SL} that is almost independent of V_{eff} and smaller than 5%. Solvents with V_{eff} below ~125 $Å^3$ have larger ΔW_{SL} with large variations among them. These results

confirm the predictive power of our model. We have tried to correlate the large variations at low V_{eff} to the properties of the solvents we used to no avail. The most likely explanation is that the work of adhesion is affected by many properties of the solvent (such as its polarity, polarizability, etc.) but thus far we could not find a single predictive property for its magnitude. To further confirm our hypothesis on the size of the molecules of the solvents, we have reviewed previously published data[18], where the solubility of nanoparticles similar to the ones studied here was evaluated in a large number of solvents. It was reported that a non-monotonic dependence of the solubility on the ligand shell composition was observed only for a subset of solvents while another subset provided solubility data that could be simply explained in terms of average hydrophobicity of the ligand shell of the nanoparticles. The paper provided no explanation on whether a solvent was part of one or the other subset. Re-evaluating those data, we find that the subset of solvent that showed a non-monotonic dependence on ligand shell composition is composed of solvents whose V_{eff} is smaller than ~130 $Å^3$, in agreement with our hypothesis (see Figure S13).

The theoretical construction, supported by the experiments and simulations, that we have reported here, represents an important step forward towards a molecular understanding of wetting. It has to be seen as an attempt to challenge the currently accepted paradigm that considers concepts like hydrophobicity as absolute. Extending these findings to more complex scenarios, such as biological systems and proteins, will require significant extensions to the experimental and theoretical approach, e.g. to account for the dynamical nature of polypeptides. The concepts and techniques we introduced here, however, lay the foundations for these studies, and for a deeper understanding of the interplay between the chemical nature and the geometric arrangement of molecular units at interfaces.

Materials and Methods

Chemicals

Chloro(triphenylphosphine)gold(I) (≥99.9% trace metals basis, Aldrich), 1-Octanethiol (≥98.5%, Aldrich), 3-Mercaptopropionic acid (HPLC, ≥99.0%, Aldrich), 3-Mercaptopropionic-2,2,3,3-d4 Acid (98 atom % D, C/D/N Isotopes Inc.), borane t-butylamine complex (97%, Aldrich), Acetone(HPLC, ≥99.8%, Aldrich), Methanol (HPLC, ≥99.9%, Aldrich), Ethanol (HPLC, ≥99.8%,

Aldrich), Chloroform (HPLC, ≥99.9%, Aldrich), Toluene (HPLC, 99.8%, Aldrich), Sulfuric acid (98.0%, Aldrich), (3-Mercaptopropyl)trimethoxysilane (95%, Aldrich), Hexane (99%, Aldrich), Iodine (≥99.99% trace metals basis, Aldrich), Tetrahydrofuran-d8 (≥99.5 atom % D, Aldrich), Chloroform-d (99.8 atom % D, Aldrich), Methanol-d4 (99.96 atom % D, Aldrich). All chemicals were used as received.

Synthesis of 1-octanethiol protected gold nanoparticles

The OT homo-ligand protected nanoparticles were synthesized following a modified protocol of Stucky and coworkers. 123 mg chloro(triphenylphosphine)gold(I) was dissolved in 40 ml 1: 1 mixture of chloroform and toluene. 0.25 mmol OT ligand was added to the solution. The mixture was heated to 70 °C for 15 minutes. Then, 217 mg borane t-butylamine complex was added quickly into the solution under stirring. The color of the solution changed from brown to dark red. After 1 hour of reaction, 40 ml methanol was added to quench the reaction and the solution was cooled down to room temperature. Nanoparticles were precipitated as black powder and purified by repeated centrifugation using acetone and methanol. The final black precipitates (~40 mg) were dried under vacuum overnight.

Synthesis of MPA-OT mixed ligand gold nanoparticles by ligand exchange reaction

40 mg OT homo-ligand protected nanoparticles were dissolved in 20 ml chloroform. 2.3 ul MPA was added to the solution under vigorous stirring. After 6 hours of reaction at room temperature, 20 ml toluene was added to precipitate the nanoparticles. The precipitate was washed multiple times using chloroform and toluene, and then dried under vacuum overnight.

Thermo-treatment of MPA-OT mixed ligand nanoparticles

20 mg MPA-OT nanoparticles was dissolved in 5 ml ethanol (containing 0.01% v/v sulfuric acid). The solution was heated at 70°C under stirring for 4 hours before cooled down to room temperature. Then the nanoparticles were precipitated by adding 30 ml hexane and washed using chloroform before being dried under vacuum overnight.

Small angle neutron scattering

SANS measurements were conducted on the SANS-I instrument at Paul Scherrer Institute and further confirmed on KWS-2 instrument at Jülich Center for Neutron Science. For both measurements, a nanoparticle solution at a concentration of 10 mg/ml were used corresponding to a volume fraction of less than 0.1%. Measurements at SANS-1 were performed at 20 °C, using 1.5 m sample-to-detector distance, at 5 Å wavelength with a collimation setup of 6 m covering a q range from 0.03 $Å^{-1}$ to 0.5 $Å^{-1}$. Similarly, measurements on KWS-2 were performed at 20 °C, using 1.7 m sample-to-detector distance, at 4.7 Å wavelength with a collimation setup of 8 m and a q range from 0.03 $Å^{-1}$ to 0.5 $Å^{-1}$. The data acquisition time was 2 hours for each sample. The two-dimensional scattering data were processed and reduced using BerSANS or QtiKWS software for the radial averaging, background subtraction, transmission correction, and normalization to the absolute scale.

SAXS

SAXS measurements were performed using Rigaku BioSAXS 2000. Both nanoparticles were dissolved in ethanol (containing 0.1% H_2SO_4 to protonate the MPA ligands in order to gain better colloidal stability) with a concentration of approximately 0.1mg/ml. Soda lime glass capillaries with inner diameter 1.0 mm and wall thickness of 0.01 mm was used for the measurements. The data acquisition time is 2 hours for each sample. The SAXS data were fitted using SasView software by a core-shell sphere model assuming Gaussian distribution.

TEM

TEM images were taken using FEI Tecnai Osiris instrument at an accelerating voltage of 120 kV. The nanoparticle samples were prepared by drop-casting 2 µl of the above mentioned ethanol solution (0.1mg/ml) onto the carbon coated - copper 400 mesh grid following by drying under ambient condition.

NMR

NMR spectra were recorded using Bruker 400MHz spectrometer. In order to determine the ligand ratio on nanoparticle surfaces, 5 mg nanoparticles were first dissolved in 0.5 ml deuterated methanol solvent and ^1H NMR spectra were then taken to make sure that no sharp peaks corresponding to unbounded small organic molecules exist. Then 0.1 ml deuterated methanol

solution of iodine with a concentration of 50 mg/ml was added into the nanoparticle solution to etch the core of nanoparticles. After the etching of the gold core, the solution is filtered and ^{1}H NMR spectra were taken again to determine the ligand ratio on nanoparticle surfaces.

TGA

TGA measurements were done using TGA 4000 instrument from Perkin Elmer. Around 15 mg of nanoparticle samples were used. The glow of nitrogen gas is at 20.0 ml/min. The samples were heated from 50°C to 750°C, at 5.0 C/min.

FTIR

The 6700 Nicolet instrument from Thermo Fischer Scientific was used for measuring the IR spectra. Nanoparticle ethanol solution of 10 mg/ml was drop-casted on the ATR crystal and dried completely. 512 spectra were taken at 2 cm^{-1} resolution and averaged for each sample. Baseline correction was performed using the OMNIC software.

Contact angle

Glass slides were first repeatedly cleaned using ethanol and acetone to remove surface contaminants. Then they were immersed in freshly prepared base solution, sonicated for 3 minutes and rinsed with deionized water and ethanol before being dried under vacuum. The film of nanoparticles (formed at the water-air interface) was deposited on the glass slide. The procedure was repeated three times, letting the film dry in between consecutive depositions. The slides were then completely dried under vacuum before the contact angle measurements. Contact angle were measured using DataPhysics OCA 35 Instruments. More than 10 drops of 5 µl were deposited on different sites of the substrates.

For contact angle measurements of different organic solvents, the water contact angle of the nanoparticle films was first measured to make sure that the same results were reproduced, i.e. the films have the same roughness. For each solvent, at least 3 drops of 2 µl were deposited on different sites of the substrates. All the measured contact angle data as well as the solvent properties are listed in Table S4.

SFG

The sample preparation was performed as described below: the CaF_2 window was cleaned with ethanol and ultrapure water. The nanoparticle ethanol solution (prepared as described above, 0.1 mg/ml) was drop casted on top of the CaF_2 window. After solvent evaporation the window was finally flushed with argon, just before the measurement. 25 µl of D_2O were added on top of the nanoparticle film in a sample cuvette with a path length of 0.2 mm.

Vibrational SFS spectra were recorded using the setup for SFG experiments described in (24). An 800 nm regeneratively amplified Ti: sapphire system (Spitfire Pro, Spectra physics) seeded with an 80MHz 800 nm oscillator (Integral 50, Femtolasers) was operated at a 1 kHz repetition rate to pump a commercial OPG/OPA/DPG system (HE-TOPAS-C, Light Conversion), which was used to generate infrared pulses. The visible beam was split off directly from the amplifier, and spectrally shaped with a home-built pulse shaper. The angle between the 10 mJ visible (VIS) beam (800 nm, FWHM 15 cm) and the 6 mJ infrared beam (3–4.5 mm, FWHM 160 cm1) was 20 (as measured in air). The focused laser beams were overlapped in the sample cuvette. The reflected SF light was collimated using a plano-convex lens (f.15 mm, Thorlabs LA1540-B) and passed through two short-wave pass filters (3rd Millenium, 3RD770SP). The SF light was spectrally dispersed with a monochromator (Acton, SpectraPro 2300i) and detected with an intensified CCD camera (Princeton Instruments, PI-Max3) using a gate width of 10 ns. The acquisition time for a single spectrum was 150 s. A Glan-Taylor prism (Thorlabs, GT15-B), a half-wave plate (EKSMA, 460-4215) and a polarizing beam splitter cube (CVI, PBS-800-050) and two BaF2 wire grid polarizers (Thorlabs, WP25H-B) were used to control the polarization of the SFG, VIS and infrared beams, respectively.

All measurements were performed in the SSP polarization combination. The optical path was closed in a box filled with nitrogen, in order to reduce absorption from CO_2. The collection of the full spectra was achieved by combining multiple spectra collected shifting the frequency of the IR beam by 200 cm^{-1} every time.

AFM

The sample preparation for AFM is similar to the one for contact angle described above except for the fact that the glass slides where functionalized before the deposition of the nanoparticles: 50 mM (3-mercaptopropyl)trimethoxysilane acetone solution was used to immerse the slides for 4 hours in order to functionalize the surface. The glass surfaces were then rinsed multiple times with ethanol and deionized water and the nanoparticle film was deposited as described above. The samples were then completely dried under vacuum. Multiple glass slides were attached to the same metal disc (TED PELLA) using the wax Apiezon 100. In this way, it was possible to move from one sample to the other during the experiment without unmounting the sample cell in the AFM.

Atomic force microscopy images were collected in amplitude modulation mode on a commercial Cypher ES system (Asylum Research/Oxford Instruments, Santa Barbara, CA). The temperature was kept constant at 25 °C during all the measurements. The sensitivity of the cantilevers (RC800 PSA, lever number 1, Olympus, Tokyo, Japan) was evaluated from force curves and the spring constant was measured from their thermal spectra. The cantilevers were driven acoustically. Typical scan rates were in the range 5-13 Hz.

The values of the free amplitude and free phase of oscillation where extracted from dynamic force curves collected immediately after high resolution imaging was achieved.

Simulation Details

All simulations were carried out using the GROMACS/2018.4 software package(28), with the OPLS/AA forcefield(29) used to describe inter-ligand interactions, the SPC/E model(30) for water and the GolP model for the gold surface(31). In all simulations, a gold slab with height 5 nm is placed at the centre of the simulation box, ligands attached to the surface (with the positions of the sulfur atom of each ligand fixed throughout each simulation, as were all gold atoms other than the image-charge sites(31) and 5 nm slabs of water placed above and below the gold surface and allowed to condense onto the ligands. Further details of the simulation setup and running are given in the Supplementary Discussion.

The structure of the solvent around the nanoparticle surface was quantified using two properties: the density ρ, obtained by taking a histogram of coordinates of the oxygen atoms in water

519 molecules, and the dipole orientation density $\mu = \langle\cos\theta\rangle\rho$, where $\langle\cos\theta\rangle$ is the average orientation
520 of the water dipole moment with the surface normal pointing away from the gold surface.

521
522 **Acknowledgments:** Z.L, Q.K.O. and F.S. gratefully acknowledge funding from the Swiss
523 National Foundation Division II. A.M. acknowledges the support from the Marie Slodowska-Curie
524 ITN project iSwitch (GA-642196). F.K and H.I.O. acknowledge funding from the Swiss federal
525 government agency (SERI) thanks to the EU H2020-MSCA-ITN project iSwitch (Grant
526 Agreement No. 642196). M.C and D.M.W. acknowledge funding from the European Research
527 Council under the European Union's Horizon 2020 research and innovation programme (grant
528 agreement no. 677013-HBMAP). The authors are grateful to PSI and JCNS for kindly providing
529 valuable beam times. We thank Dr. Sandor Balog for helping with SAXS measurements. We thank
530 the helpful discussion with Dr. Kislon Voïtchovsky, Dr. Nikolay Smolentsev, Dr. Nikolaos Nianias,
531 Jan Dedic, Andrea Anelli and Walter Scholdei.

References

1. M. L. Connolly, Solvent-accessible surfaces of proteins and nucleic acids. *Science* **221**, 709 LP – 713 (1983).

2. A. B. D. Cassie, Contact angles. *Discussions of the Faraday Society* **3**, 11–16 (1948).

3. M.-C. Bellissent-Funel, *et al.*, Water Determines the Structure and Dynamics of Proteins. *Chemical Reviews* **116**, 7673–7697 (2016).

4. C. A. Silvera Batista, R. G. Larson, N. A. Kotov, Nonadditivity of nanoparticle interactions. *Science* **350** (2015).

5. K. A. Dill, Additivity Principles in Biochemistry. *Journal of Biological Chemistry* **272**, 701–704 (1997).

6. S. Simm, J. Einloft, O. Mirus, E. Schleiff, 50 years of amino acid hydrophobicity scales: revisiting the capacity for peptide classification. *Biological Research* **49**, 31 (2016).

7. E. Xi, *et al.*, Hydrophobicity of proteins and nanostructured solutes is governed by topographical and chemical context. *Proceedings of the National Academy of Sciences of the United States of America* **114**, 13345–13350 (2017).

8. N. Giovambattista, P. G. Debenedetti, P. J. Rossky, Hydration behavior under confinement by nanoscale surfaces with patterned hydrophobicity and hydrophilicity. *Journal of Physical Chemistry C* **111**, 1323–1332 (2007).

9. N. Giovambattista, C. F. Lopez, P. J. Rossky, P. G. Debenedetti, Hydrophobicity of protein surfaces: Separating geometry from chemistry. *Proceedings of the National Academy of Sciences of the United States of America* **105**, 2274–2279 (2008).

10. H. Acharya, S. Vembanur, S. N. Jamadagni, S. Garde, Mapping hydrophobicity at the nanoscale: Applications to heterogeneous surfaces and proteins. *Faraday Discussions* **146**, 353–365 (2010).

11. C. T. Nguyen, M. Barisik, B. Kim, Wetting of chemically heterogeneous striped surfaces: Molecular dynamics simulations. *AIP Advances* **8**, 065003 (2018).

12. J. J. Kuna, *et al.*, The effect of nanometre-scale structure on interfacial energy. *Nature materials* **8**, 837–842 (2009).

13. C. D. Ma, C. Wang, C. Acevedo-Vélez, S. H. Gellman, N. L. Abbott, Modulation of hydrophobic interactions by proximally immobilized ions. *Nature* **517**, 347–350 (2015).

14. S. Chen, *et al.*, Subnanoscale hydrophobic modulation of salt bridges in aqueous media. *Science* **348**, 555–559 (2015).

15. N. Giovambattista, P. G. Debenedetti, P. J. Rossky, Hydration behavior under confinement by nanoscale surfaces with patterned hydrophobicity and hydrophilicity. *Journal of Physical Chemistry C* **111**, 1323–1332 (2007).

16. C. Singh, *et al.*, Entropy-mediated patterning of surfactant-coated nanoparticles and surfaces. *Physical Review Letters* **99**, 226106 (2007).

17. Q. K. Ong, *et al.*, High-resolution scanning tunneling microscopy characterization of mixed monolayer protected gold nanoparticles. *ACS Nano* **7**, 8529–8539 (2013).

18. A. Centrone, *et al.*, The role of nanostructure in the wetting behavior of mixed-monolayer-protected metal nanoparticles. *Proceedings of the National Academy of Sciences* **105**, 9886–9891 (2008).

19. Z. Luo, J. Hou, L. Menin, Q. K. Ong, F. Stellacci, Evolution of the Ligand Shell Morphology during Ligand Exchange Reactions on Gold Nanoparticles. *Angewandte Chemie - International Edition* **56**, 13521–13525 (2017).

20. A. Centrone, Y. Hu, A. M. Jackson, G. Zerbi, F. Stellacci, Phase separation on mixed-monolayer-protected metal nanoparticles: A study by infrared spectroscopy and scanning tunneling microscopy. *Small* **3**, 814–817 (2007).

21. Z. Luo, *et al.*, Quantitative 3D determination of self-assembled structures on nanoparticles using small angle neutron scattering. *Nature Communications* **9**, 1343 (2018).

22. Q. Ong, Z. Luo, F. Stellacci, Characterization of Ligand Shell for Mixed-Ligand Coated Gold Nanoparticles. *Accounts of Chemical Research* **50**, 1911–1919 (2017).

23. L. E. Marbella, J. E. Millstone, NMR techniques for noble metal nanoparticles. *Chemistry of Materials* **27**, 2721–2739 (2015).

24. N. Smolentsev, W. J. Smit, H. J. Bakker, S. Roke, The interfacial structure of water droplets in a hydrophobic liquid. *Nature Communications* **8**, 15548 (2017).

25. K. Voïtchovsky, J. J. Kuna, S. A. Contera, E. Tosatti, F. Stellacci, Direct mapping of the solid–liquid adhesion energy with subnanometre resolution. *Nature Nanotechnology* **5**, 401 (2010).

26. J. Z. Liu, A. van de Walle, G. Ghosh, M. Asta, Structure, energetics, and mechanical stability of Fe-Cu bcc alloys from first-principles calculations. *Phys. Rev. B* **72**, 144109 (2005).

27. A. Díaz-Ortiz, H. Dosch, R. Drautz, Cluster expansions in multicomponent systems: precise expansions from noisy databases. *J. Phys.: Condens. Matter* **19**, 406206 (2007).

28. M. J. Abraham, *et al.*, GROMACS: High performance molecular simulations through multi-level parallelism from laptops to supercomputers. *SoftwareX* **1–2**, 19–25 (2015).

29. M. J. Robertson, J. Tirado-Rives, W. L. Jorgensen, Improved Peptide and Protein Torsional Energetics with the OPLS-AA Force Field. *J. Chem. Theory Comput.* **11**, 3499–3509 (2015).

30. H. J. C. Berendsen, J. R. Grigera, T. P. Straatsma, The missing term in effective pair potentials. *J. Phys. Chem.* **91**, 6269–6271 (1987).

31. F. Iori, R. Di Felice, E. Molinari, S. Corni, GolP: an atomistic force-field to describe the interaction of proteins with Au(111) surfaces in water. *J Comput Chem* **30**, 1465–1476 (2009).

Author contributions: Z.L. synthesized the nanoparticles; Z.L., J.K., A.R. and Q.K.O. characterized the nanoparticles; A.M., Z.L., F.K. and H.I.O performed the SFG measurements under the supervision of S.R.; A.M. and Z.L. measured AFM and contact angle on the nanoparticles; D.M.W. performed the molecular dynamic studies under the supervision of M.C.; Z.L., A.M., D.M.W., M.C., and F.S. designed research and prepared the manuscript.

Supplementary Information

Determination and Evaluation of the Non-Additivity in Wetting of Molecularly Heterogeneous Surfaces

Zhi Luo,[1]† Anna Murello,[1]† David M. Wilkins,[1]† Filip Kovacik,[2] Joachim Kohlbrecher,[3] Aurel Radulescu,[4] Halil I. Okur,[2] Quy K. Ong,[1] Sylvie Roke,[1,2] Michele Ceriotti,[1] Francesco Stellacci[1,2*]

[1]Institute of Materials, École Polytechnique Fédérale de Lausanne, 1015 Lausanne, Switzerland.

[2]Institute of Bioengineering, École Polytechnique Fédérale de Lausanne, 1015 Lausanne, Switzerland.

[3]Laboratory for Neutron Scattering and Imaging, Paul-Scherrer Institut, 5232 Villigen, Switzerland.

[4]Forschungszentrum Jülich Gmbh, Jülich Center for Neutron Science, JCNS at Heinz Maier-Leibnitz Zentrum, Lichtenbergstraße 1, 85747 Garching, Germany.

†These authors contributed equally to this work.

*Correspondence to: francesco.stellacci@epfl.ch

Supplementary Discussion

Effect of deuteration on the ligand shell nanoparticles

In the current work, most of the data i.e. SANS, SAXS, FTIR, TEM, SFG, AFM, and Contact angle, were measured on the same batches of nanoparticles, i.e. NPs coated with dMPA and OT. For the measurements of NMR and TGA, we used NPs coated with MPA and OT due to the requirements of the techniques. All the nanoparticles were synthesized using ligand exchange reaction from the same batch of OT homoligand NPs. Therefore, they should have the same core size and size distribution. For the ligand shell composition, we have previously shown that the deuteration does not affect the ligand shell composition for the same(1) and similar(2) type of ligand coated NPs. Furthermore, while for the SANS modelling, only 50% penalty was imposed on the volume fraction of the ligands, i.e. the ligand shell ratio was not fixed. The volume ratio of the outcome model is MPA: OT = 1: 2.12. While the ligand ratio from NMR measurements is MPA: OT= 55%: 45%, which corresponds to approximately MPA: OT= 1: 2.18, agreeing well with the resulted 3D model. The good quality of the fits also confirms that the ligand ratios are consistent with NMR data.

Ab initio model fitting of SANS data

As described in a recent report, the construction of 3D models from SANS data was performed using MONSA software(3). Briefly, a spherical search volume with a diameter of 7.2 nm was generated according to the pair distribution function calculated using GNOM(4) program. The search volume composed of closely packed beads with a radius of 2 Å. Each bead could be assigned either to the gold, MPA, OT or solvent phase. To facilitate the calculation, the beads within 2 nm radius are fixed to be gold, while beads between 2.7 nm 3.6 nm radius could be assigned to either the two types of ligands or solvent. The ratio of volume fraction of the two types of ligands, calculated from the NMR and TGA value (OT: MPA= 2.0: 1), was used as a fitting penalty during the simulated annealing process. Starting from random configurations, simulated annealing was conducted in order to minimize the discrepancy between the experimental data and the form factor of the bead model. The discrepancy is defined as:

$$\chi^2 = \sum_k \frac{1}{N_k - 1} \sum_{j=1}^{N_k} \left[\frac{I_{\exp}^{(k)}(q_j) - c_k I_{\text{calc}}^{(k)}(q_j)}{\sigma^{(k)}(q_j)} \right]^2$$

Where, the k is the index of scattering curves; N_k is the number of points in the experimental scattering curves; $I_{exp}(q)$ and $I_{calc}(q)$ are the intensities from the experiments and the calculation of the bead model; c_k is the scale factor and $\sigma(q)$ is the experimental errors at each q.

The model fitting process was repeated multiple times always starting from random configurations and the resulting models all present similar ligand shell organization features.

Interpretation of the C-H region of SFG spectra

Since the morphological evolution during the annealing is driven by the gain in conformational entropy of the OT ligands, one would expect for the stripe-like NPs a higher gauche to trans ratio for the ligands compared to the patchy one. To measure such conformational changes, we performed SFG measurements also in the C-H stretch region (2800 – 3000 cm^{-1}) of the vibrational spectrum of NPs as shown in Figure S5. The ligand MPA was deuterated so that only the conformation of the OT was probed. Using SFG the alkyl chain conformations can be determined empirically using the amplitude ratio (referred to as d^+/r^+ ratio) of the symmetric methylene (~2850 cm^{-1}, d^+) and the symmetric methyl (~2880 cm^{-1}, r^+) stretch vibrational modes. A value of $d^+/r^+ \ll 1$ is associated with a stretched all-trans alkyl chain conformation, whereas a value of $d^+/r^+ > 1$ indicates that gauche defects dominate the measured vibrational spectrum(5–7). The SFG spectra of both NPs display a different relative amplitude of the d^+ and r^+ mode indicating that the average ligand conformation on the NPs is different. The stripe-like nanoparticle displays a larger d^+/r^+ indicating less stretched alkyl chains.

Work of adhesion measurement from AFM

Images were collected working in the small-amplitude regime in order to map the work(8). The formula proposed in literature to estimate the work of adhesion from the imaging parameters is the following:

$$W_{SL} = a + b\left[\frac{AA_0\left(sin\varphi - \frac{A}{A_0}\right)}{e^{\frac{-\alpha\sigma}{2}} - e^{\frac{-\alpha(A+\sigma)}{2}}}\right]^2,$$

where A is the working amplitude, A_0 is the free amplitude, φ is the phase shift, σ is the molecular diameter of the liquid and α is the exponential decay length of the density of work of adhesion at the solid-liquid interfaces.

The method does not provide an absolute measurement, but only a relative one that needs to be calibrated through the measurement of contact angle on reference samples. In fact, since the energy dissipation is calculated with respect to the oscillation of the cantilever in the bulk liquid, the intercept of the calibration line is always given by the surface tension of the imaging liquid, thereof only one reference sample is needed for the calibration. We used a film of MPA protected gold nanoparticles as a calibration system for the measurement of the W_{SL} for the patchy NPs. The value of the work of adhesion calculated for these particles was then used as a calibration system for the stripe-like NPs.

To get a reliable comparison of different samples (and hence a good calibration), the exact same A_0 was kept while scanning different samples (differences ≤ 0.05 nm where considered negligible), meanwhile A was kept as constant as possible. Furthermore, images were compared only if collected in the same day and with the same tip.

Each experiment was reproduced twice. A minimum of five nanoparticles per sample were analyzed. Analysis was performed on single particles, extracted from images similar to the ones shown in Figure S7. Data analysis was performed by calculating the average value (and the standard deviation) of $f(A, A_0, \varphi)$ over all the pixels of a single particle masked from an image. This value was then used to calculate the work of adhesion (after the calibration of the system was performed. In the calibration we used 72 mN/m for the surface tension of water).

For every experiment the average value of W_{SL} on different particles and its standard deviation σ was calculated. 5 mN/m were added to each standard deviation in order to take into account the error associated with the calibration ($\sigma^* = \sigma + 5\, mN/m$). The average value for different experiments has been calculated and the final standard deviation has been obtained by propagating the σ^* of the single experiments.

Simulation details

All simulations were carried out using the GROMACS/2018.4 software package(9). Inter-ligand interactions were treated using the OPLS/AA forcefield(10), the SPC/E model(11) was used for water, and the gold surface was described with the GolP model(12). For the patchy and stripe-like surfaces, we started with a box size of ~6 nm x 6 nm in the xy plane, with a height of 30 nm. A gold (111) surface with height 5 nm was placed at the center, and ligands

attached to the surface (the positions of the sulfur atom of each ligand were constrained throughout the simulation, as were all gold atoms other than the image-charge sites(12)). Slabs of water with height 5 nm were placed above and below the ligand surfaces and allowed to condense onto the surface. For the trench surfaces, a similar procedure was followed but with the dimensions of the box 12.1 nm x 2.6 nm in the xy plane. This gives 24 columns of ligands, from which we created trenches containing 0, 1, 2, 4, 8, 12, 16, 20, 22, 23 and 24 columns of MPA ligands (an example of the simulation setup for the trenches is shown in figure S9). Surfaces with random motifs were simulated in boxes with the same dimension as the patchy and striped surfaces, with 20 different sets of random ligands generated, making 40 surfaces. 24 surfaces with tailored motifs were also designed to add to the training set if required. Figure 3A shows an example of the simulation setup for a trench surface after allowing the water slabs to condense.

For every surface, four independent runs were carried out with the initial orientation of ligands about the z axis generated randomly. Simulations were run in the NVT ensemble at 300 K with a timestep of 1 fs and a velocity-rescaling thermostat used to control the temperature(13). After allowing the water slabs to condense onto the ligand surface, the system was equilibrated for 10 ns and statistics were collected over 50 ns. The water-vacuum boundaries produced by expanding the simulation box meant that the pressure was held constant at 0 bar. Long-ranged electrostatics were dealt with using the particle-mesh Ewald (PME) method(14).

The structure of the solvent around the nanoparticle surface was quantified using two properties: the density ρ, obtained by taking a histogram of coordinates of the oxygen atoms in water molecules, and the dipole orientation density $\mu = \langle\cos\theta\rangle\rho$, where $\langle\cos\theta\rangle$ is the average orientation of the water dipole moment with the surface normal pointing away from the gold surface. The surface excesses were obtained by subtracting the predicted histogram from the one observed from simulations, where the prediction was obtained by taking the profiles calculated using surfaces with either full-MPA or full-OT coverage and linearly combining them:

$$\Delta f(z) = f_{obs}(z) - [x_{OT} f_{OT}(z) + x_{MPA} f_{MPA}(z)],$$

where $f_{OT}(z)$ is the profile from the 0-MPA trench and $f_{MPA}(z)$ is the profile from the 24-MPA trench. x_{OT} and x_{MPA} are the fraction of OT and of MPA ligands respectively.

Results on trench configurations

Based on the expectation that the boundary between OT and MPA regions is responsible for the non-additive behavior observed, we ran simulations, as described in the previous section,

on a series of trench geometries, in which the length of the boundary between the two regions is kept constant, but the area of each region differs. If the boundary region alone is responsible for non-additivity, we would expect that the excess properties of interest are independent of the size of the trench, so long as it is large enough that the two boundaries do not "interact" with each other. Figure S11 shows that, indeed, while the surface excesses differ between small and large trench sizes, for large enough trenches the excesses are relatively independent of trench size. This is further borne out by Figure 3A in the main text, in which the local water density is shown in a cut across the trench, and is similarly independent of trench size for large trenches.

When investigating the local density of water, we found that the structure of water in contact with MPA ligands follows one of two regimes, where the two structures are related (in the case of a bare surface) by a 60^o rotation, as shown in Figure S10. To obtain the results in Figure 3A, we separated each surface into one or the other type of surface-water structuring, in order to avoid spuriously averaging over two different types of structure and washing-out the local water density.

These trench configurations give a qualitative idea of how the water structure depends on the size of regions of ligand, but for a quantitative picture a wider variety of surface morphologies must be considered.

Nearest-Neighbor Model for Surface Excesses

In order to predict the surface excesses on arbitrary ligands, we developed a model in which an arbitrary excess quantity $\Delta f(z)$ (either $\Delta\rho(z)$ or $\Delta\mu(z)$) is given by the linear combination,

$$\Delta f(z) = \boldsymbol{n} \cdot \boldsymbol{f}(z)$$

$$\Delta f(z) = \sum n_i \, f_i(z),$$

where the index i represents a particular ligand environment, $\mathbf{n} = \{n_i, i=1,..,M\}$ is a vector containing the number of ligands n_i of type i, with M the total number of possible environments, and $\boldsymbol{f}(z) = \{f_i(z), i=1,..,M\}$, where the functions $f_i(z)$ are to be fitted. This expansion is inspired by the cluster expansion models used to model the thermodynamic properties of multicomponent alloys in terms of local environments(15, 16), with surface excess functions used in our case rather than, e.g., energetics.

We chose to classify ligands based on their nearest neighbors, with the remainder of their surroundings providing a mean-field background. This approach was motivated by the fact that

simulations containing trenches of ligands showed the structure of water to be quite independent on the trench size above the smallest trenches, so that long-ranged effects on the local structure were minimal. The nearest-neighbor environment of a ligand is described by the six ligands surrounding it, meaning that there are 2^7=128 possible ligand plus environment combinations. Of these, many are related by rotational symmetry, and only 26 must be considered, of which the two cases where all six surrounding ligands are identical to the central one were assumed not to contribute to the excess. The remaining 24 possible motifs are shown in Figure S12, along with the fitting functions $\Delta\rho_i(z)$ and $\Delta\mu_i(z)$ corresponding to each.

These functions were obtained by taking a training set of slab systems with the ligand at each site randomly chosen, and for which the excess quantities were computed. In terms of the matrix $\boldsymbol{n}$, whose element $\boldsymbol{n}_{ji}$ gives the number of ligands of type i in the j^{th} training structure, and a vector $\boldsymbol{\Delta f}(z) = \{\Delta f_j(z), j=1,\ldots,N\}$, where $\Delta f_j(z)$ is the surface excess for the j^{th} training structure and N the total number of such structures, the vector of fitting functions is given by,

$$\Delta \boldsymbol{f}(z) = (\boldsymbol{n}^{\boldsymbol{T}}\boldsymbol{n} + \sigma^2 \boldsymbol{I})^{-1}\boldsymbol{n}^{\boldsymbol{T}}\boldsymbol{f}(z)$$

with σ^2 a regularization parameter used to avoid overfitting.

Figure S12 shows that the contribution of each motif to a given surface excess is essentially of the same order of magnitude: no particular motif is *a priori* more important than the others in determining the excess. However, the striped surfaces contain both a larger number of environments that give an excess and a larger variety of environments (with several motifs appearing almost exclusively on striped surfaces). These factors lead to more pronounced surface excesses for the striped than for the patchy surfaces.

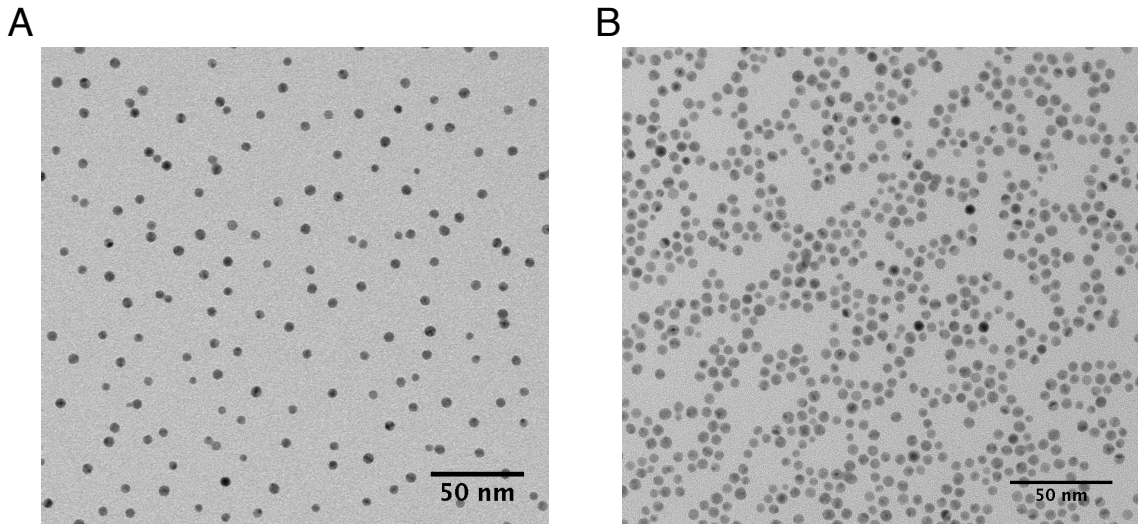

Figure S1 TEM data on the nanoparticles before (A) and after (B) thermal treatment. Based on the counting of more than 500 nanoparticles, the distributions of the core diameter are found to be 5.1 ± 0.6 nm and 5.2 ± 0.7 nm for nanoparticles before and after thermal treatment, respectively.

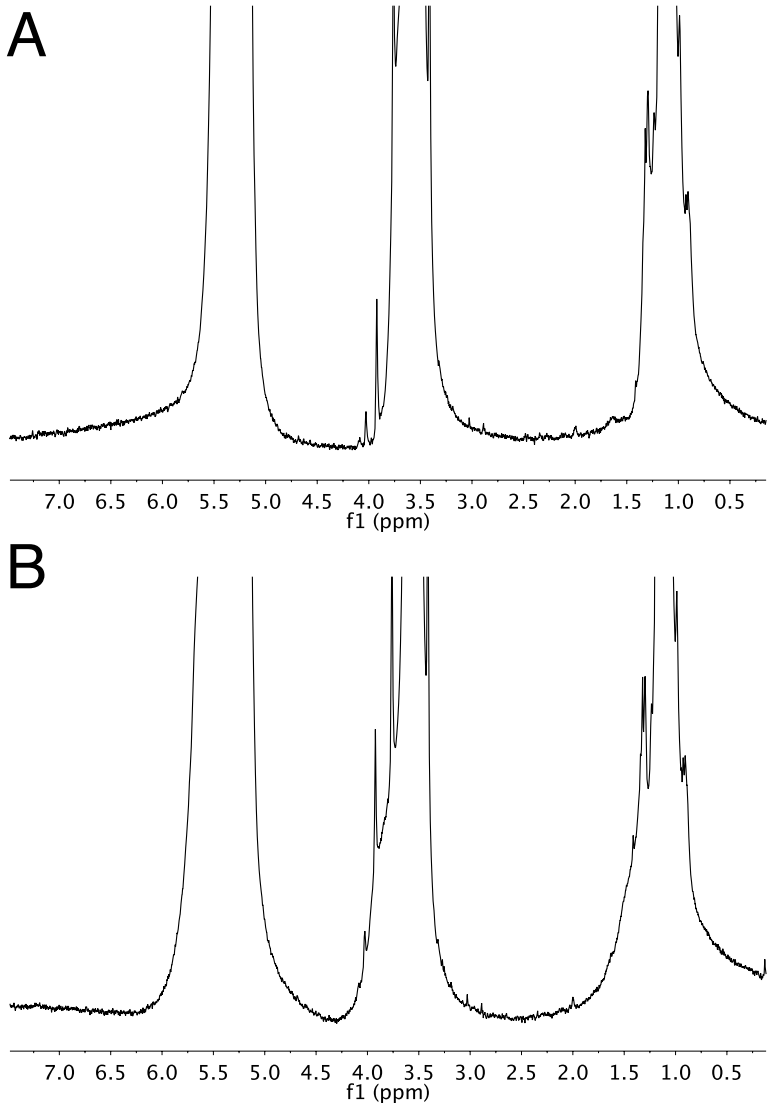

Figure S2 NMR data for nanoparticle before iodine etching. The absence of the sharp peaks between 2.5 and 3.0 ppm indicates that the nanoparticles are free from unbounded small molecules.

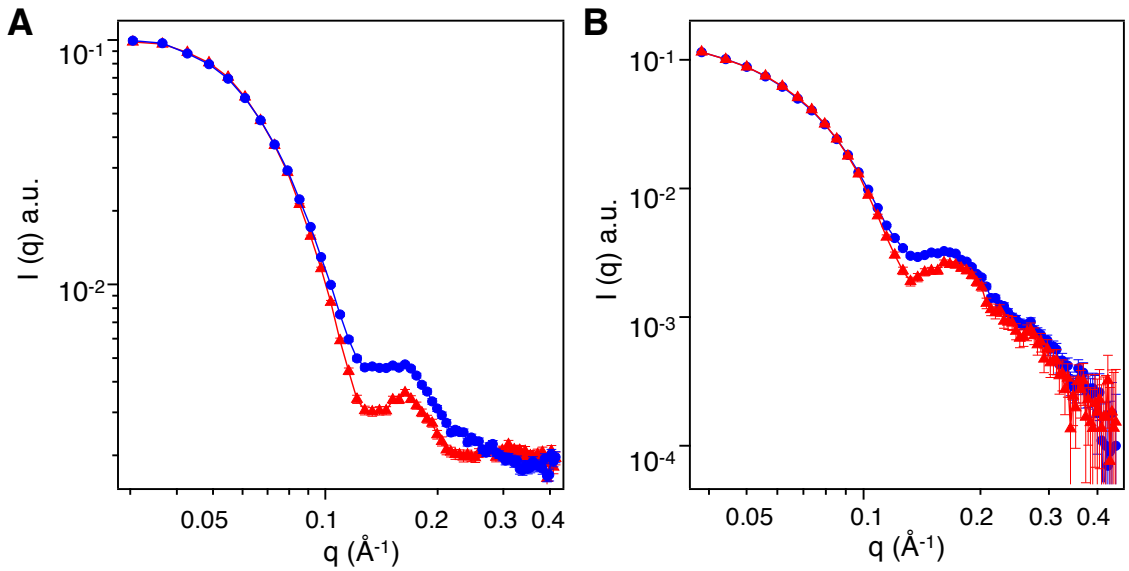

Figure S3 SANS data on the nanoparticles before and after thermal treatment measured at different synchrotron facilities. In both plots, the blue curves stand for nanoparticles before thermal treatment while the red curves stand for samples after thermal treatment. (A) Data collected at MLZ, Germany. (B) Data collected at PSI, Switzerland. The ligands for nanoparticles are the same as shown in the main text, i.e. deuterated MPA and OT.

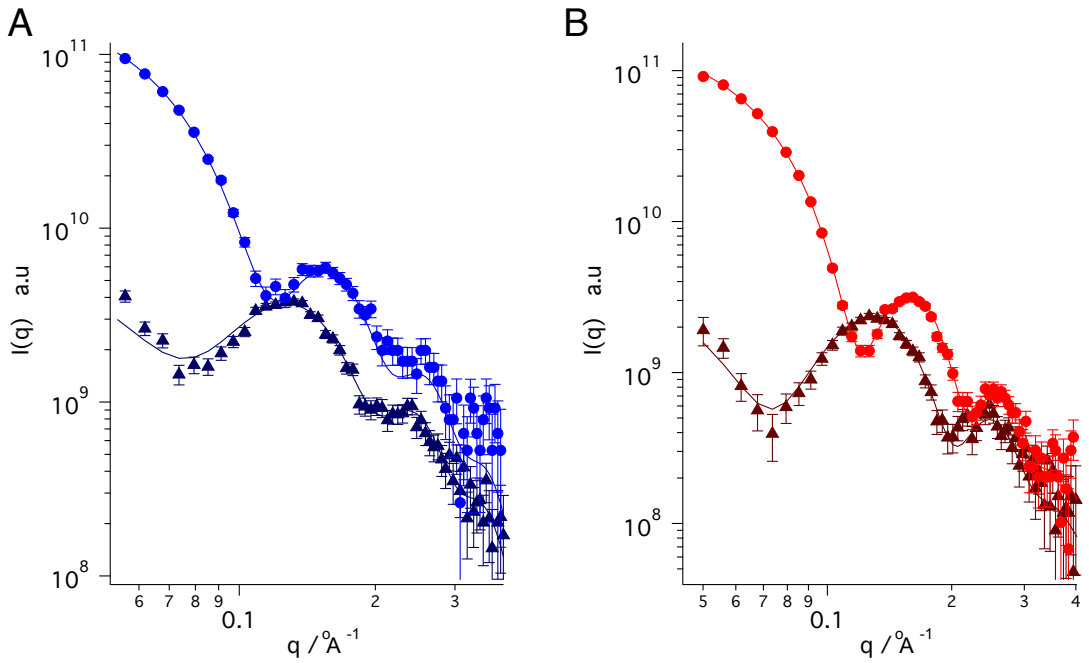

Figure S4 Fitting of the SANS data using MONSA package. In both plots, the full lines are the fits, i.e. form factor of the 3D model generated, while the dots are experimental data. (A) Nanoparticle before thermal treatment. Blue curves stand for SANS measurements in tetrahydrofuran-d8 while dark blue curves stand for SANS measurements in chloroform-d. (B) Nanoparticle after thermal treatment. Red curves stand for SANS measurements in tetrahydrofuran-d8 while dark red curves stand for SANS measurements in chloroform-d.

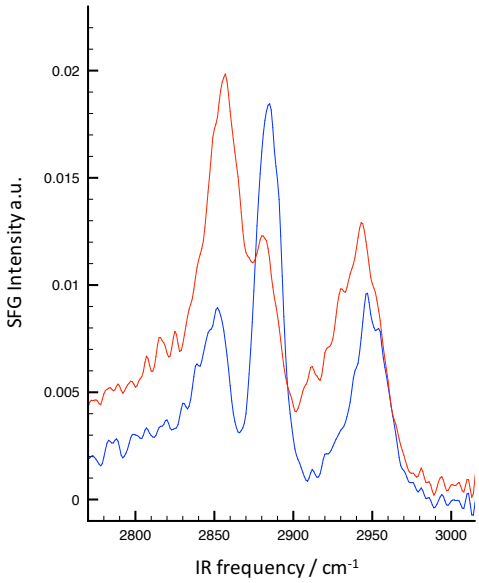

Figure S5 Representative SFG spectra in the C-H region collected in the SSP polarization. The amplitude ratio of the symmetric methylene (~ 2850 cm-1) and the symmetric methyl (~ 2880 cm-1) stretch vibrational modes are significantly different for the patchy and stripe-like particles (respectively shown with a blue and a red curves).

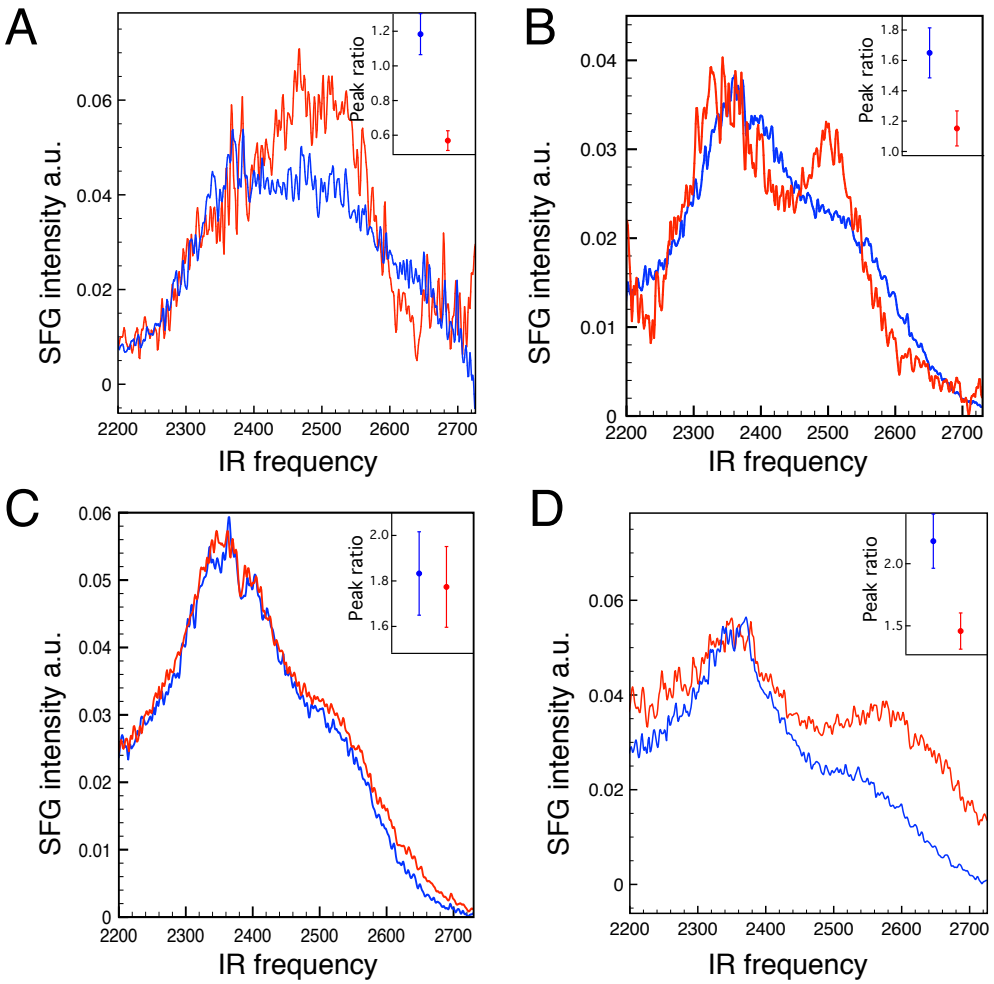

Figure S6 (A)-(D) SFG spectra in the water region, as recorded in four different measurements (Blue: patchy NPs, red: stripe-like NPs) and associated amplitude ratio of the peaks associated with the strong H bond and the weak H bond (insets). To avoid any error from laser fluctuations on different days, we choose to report our data separately. We calculated the peak to peak ratio error of the sum frequency scattering setup on 10 spectra of different samples of sodium dodecylsulfanate stabilized hexadecane nanoemulsions. and the deviation from spectrum to spectrum is less than 10 %. This value is used as an error for the values reported on the above graph. We have never observed an increase in the ratio during an experiment. The fact that during one experiment (C) we did not observe any difference between the two sets of nanoparticles can be explained by the fact that annealing may not have worked perfectly on that occasion. Since in the formation of the film it is likely that similar nanoparticles will

assemble together, it is possible that in this case the laser was focused on an area composed of nanoparticles that were not affected by annealing.

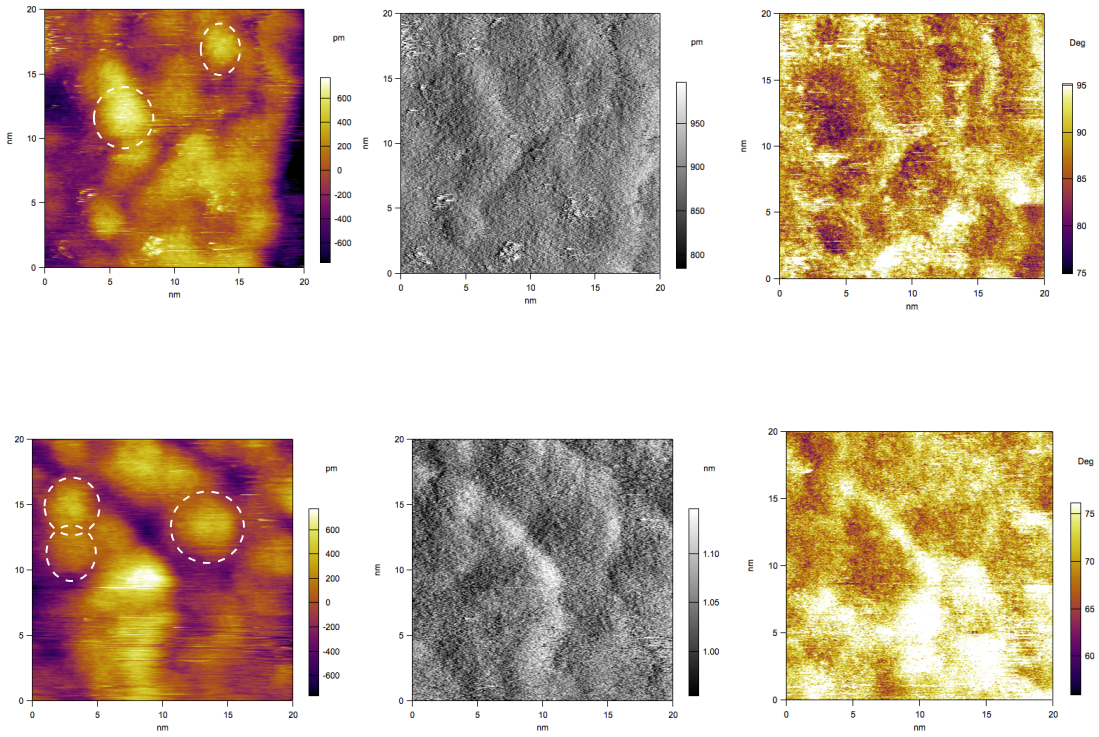

Figure S7 Representative images (in the order: height, amplitude and phase) collected on patchy NPs (top) and on stripe-like NPs (bottom). Circles indicate single particles that have been used for the calculation of W_{SL}. The value of the free phase of oscillation was 95° for the image on top and 76° for the one on the bottom.

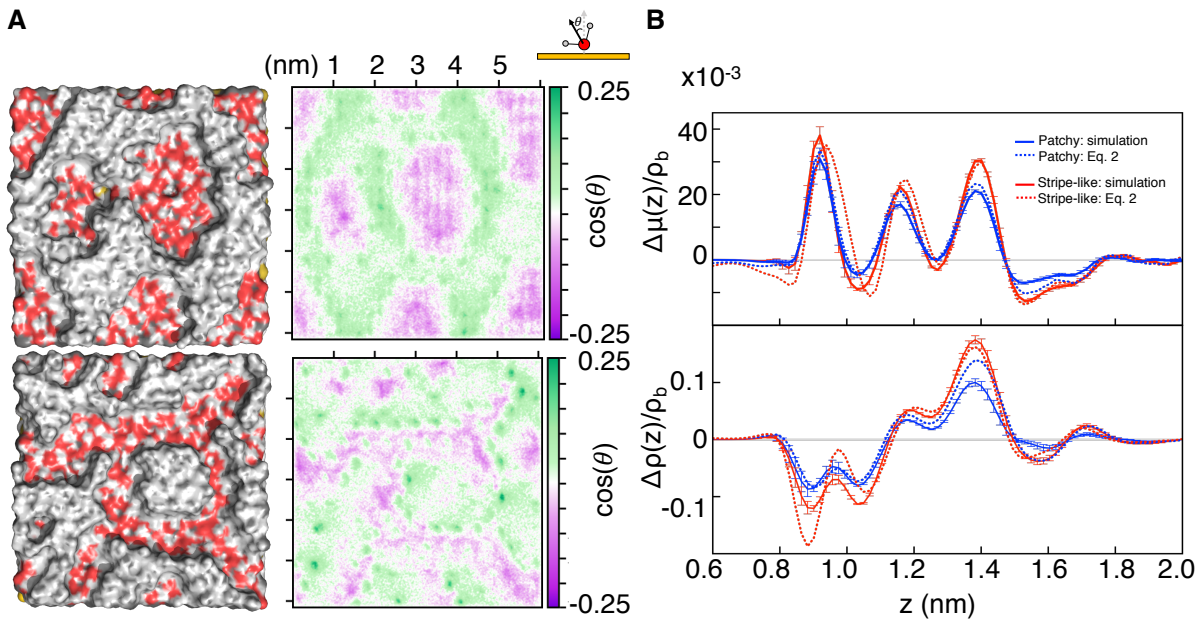

Figure S8 Reproducibility of the results of the simulations. (A) Left: morphology of two additional surfaces after equilibration (patchy on top and stripe-like on the bottom. Water molecules have been removed to show the geometry of the interface. Carbon, oxygen and hydrogen atoms are represented with grey, red and white colors respectively. Right: corresponding 2D histogram of the average dipole orientation density, μ, above the surfaces (averaged over four different realizations). Areas on top of the MPA patches look mostly purple (dipole pointing towards the surface) and areas on top of the OT patches look mostly white (dipole parallel to the surface). Green regions (dipole pointing out from the surface) are visible on top of the OT-MPA interfaces, with darker green visible on the stripe-like morphology. (B) Deviation from the additive assumption of the average dipole orientation density, Δμ, (top) and density profile of water, Δρ (bottom), as a function of the distance from the gold surface (z). Both result of the molecular dynamics simulation and the prediction from equation 2 are shown: good agreement between them is visible.

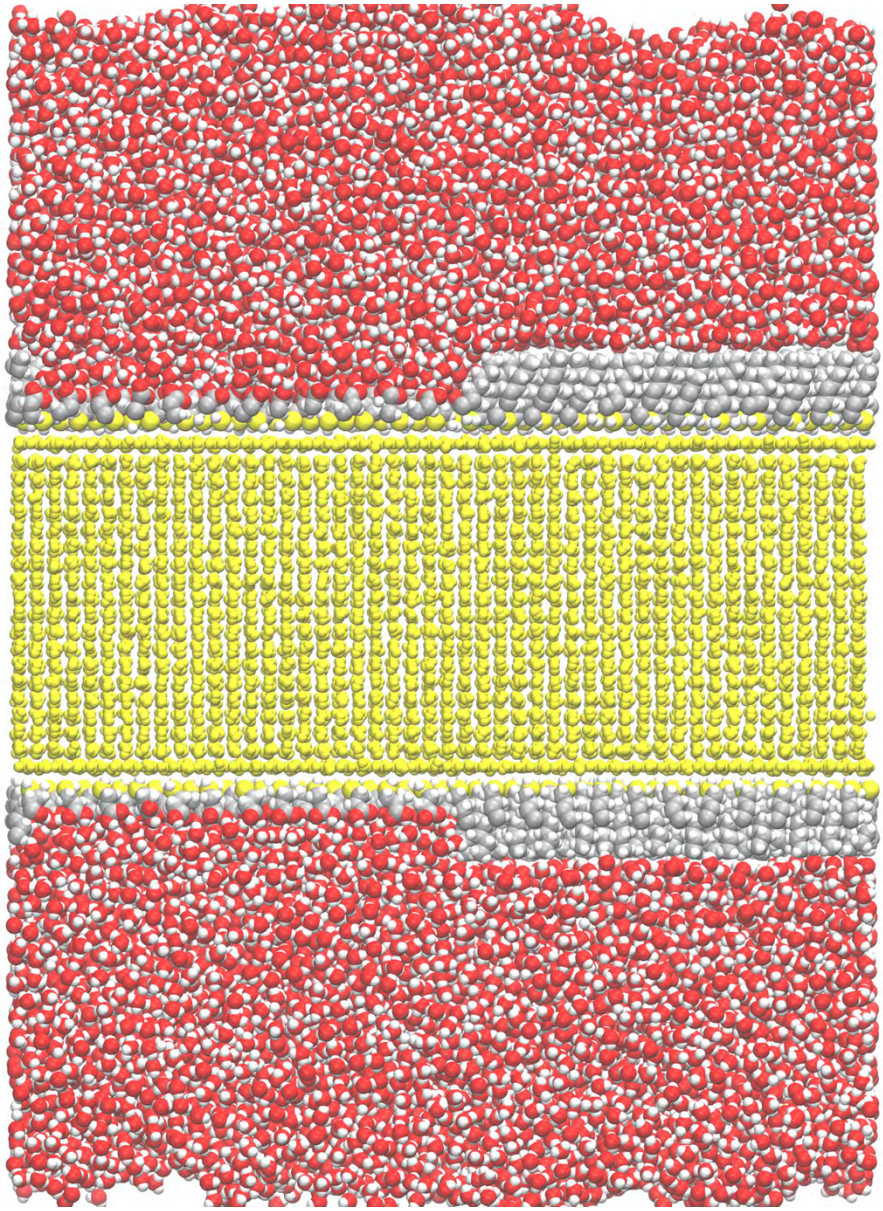

Figure S9 Illustration of the simulation setup for a trench configuration with 12 MPA and 12 OT ligands. Gold atoms are shown in yellow, carbon in grey, oxygen in red and nitrogen in white.

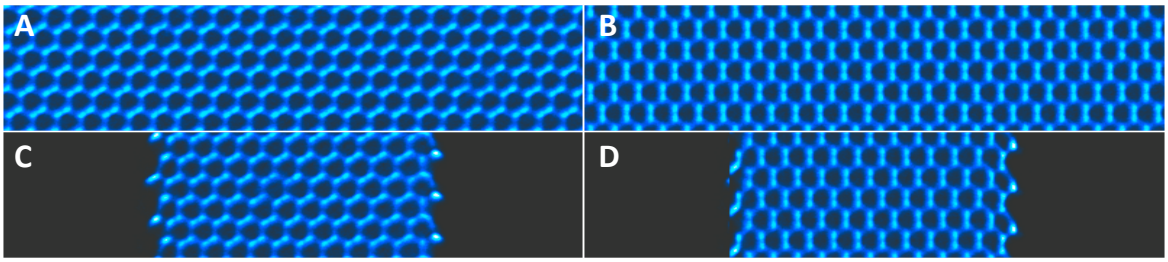

Figure S10 Water density on MPA trenches. Top row: two types of surface structure for a surface with 24 rows of MPA ligands; these are rotationally identical. Bottom row: (C) and (D) show the surface structure of water on top of the MPA ligands, equivalent to the structures in (A) and (B) respectively. Because of the presence of a region of OT ligands, these two are no longer equivalent.

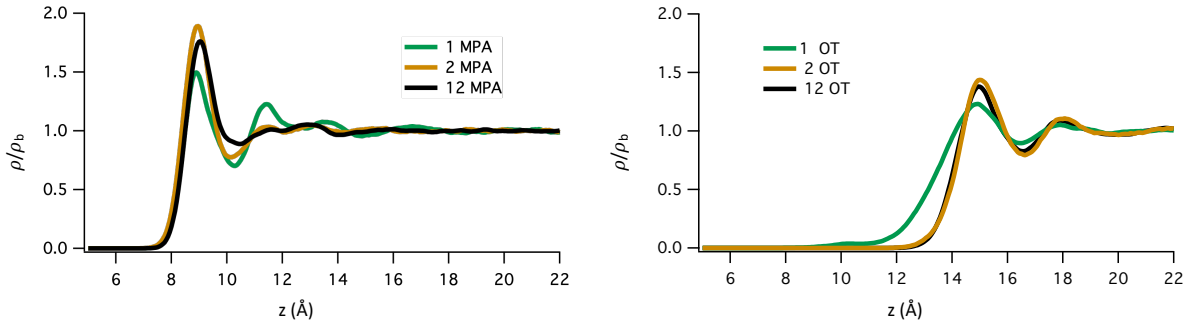

Figure S11 Density profile of water as a function of the distance from the gold surface at the center of a trench. Values measured at the center of the MPA and OT trenches are shown on the left-hand side and right-hand side respectively. In both cases the density of water on the 2 molecules thick trench (brown) is comparable with the one on the center of the 12 molecule thick trench (black). On the contrary the density of water on the single-molecule thick trench (green) looks significantly different from the trench that is 2 molecules thick.

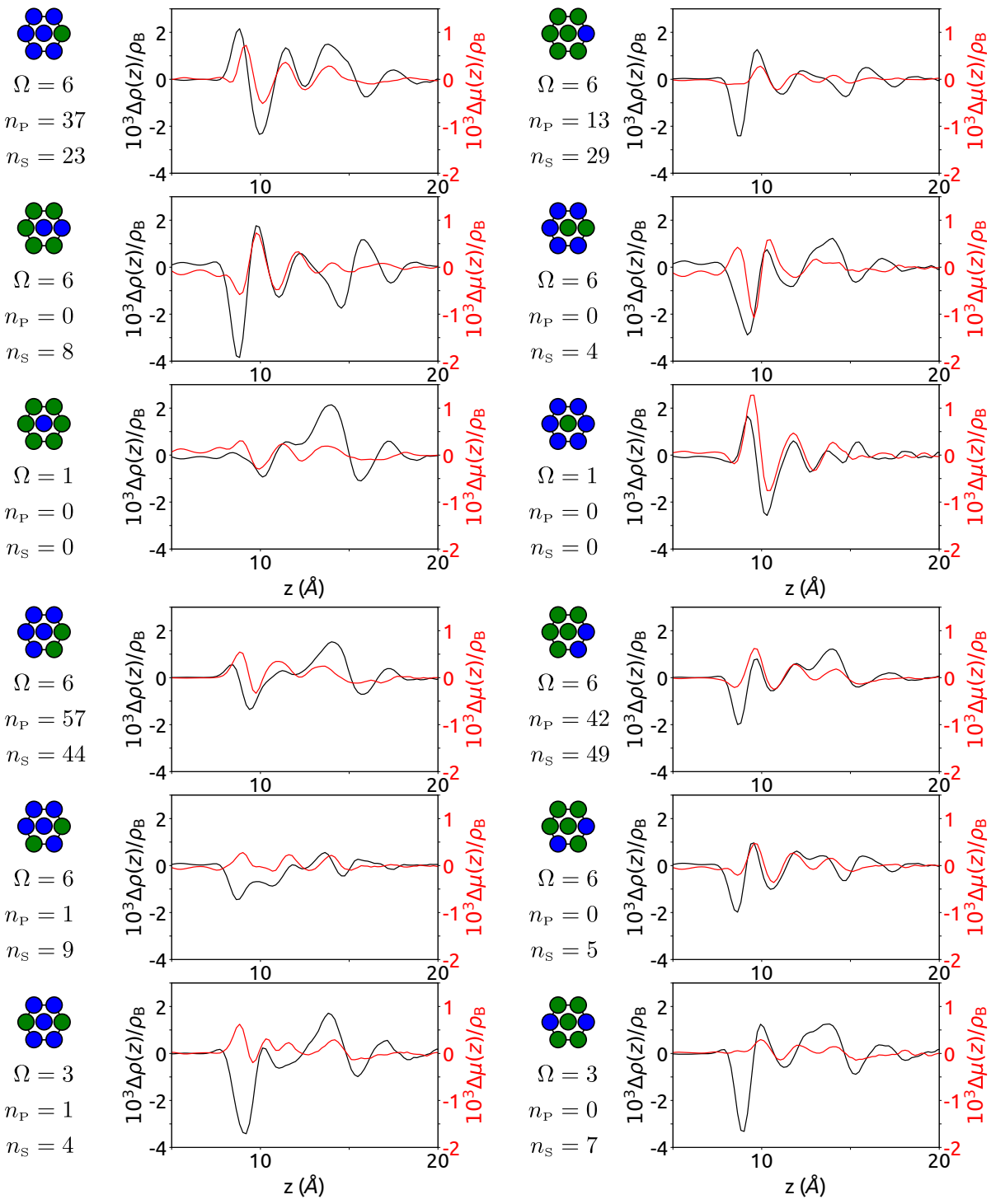
Ω = 6
n_P = 37
n_S = 23
Ω = 6
n_P = 13
n_S = 29
Ω = 6
n_P = 0
n_S = 8
Ω = 6
n_P = 0
n_S = 4
Ω = 1
n_P = 0
n_S = 0
Ω = 1
n_P = 0
n_S = 0
Ω = 6
n_P = 57
n_S = 44
Ω = 6
n_P = 42
n_S = 49
Ω = 6
n_P = 1
n_S = 9
Ω = 6
n_P = 0
n_S = 5
Ω = 3
n_P = 1
n_S = 4
Ω = 3
n_P = 0
n_S = 7
10^3Δρ(z)/ρ_B
10^3Δμ(z)/ρ_B
z (Å)

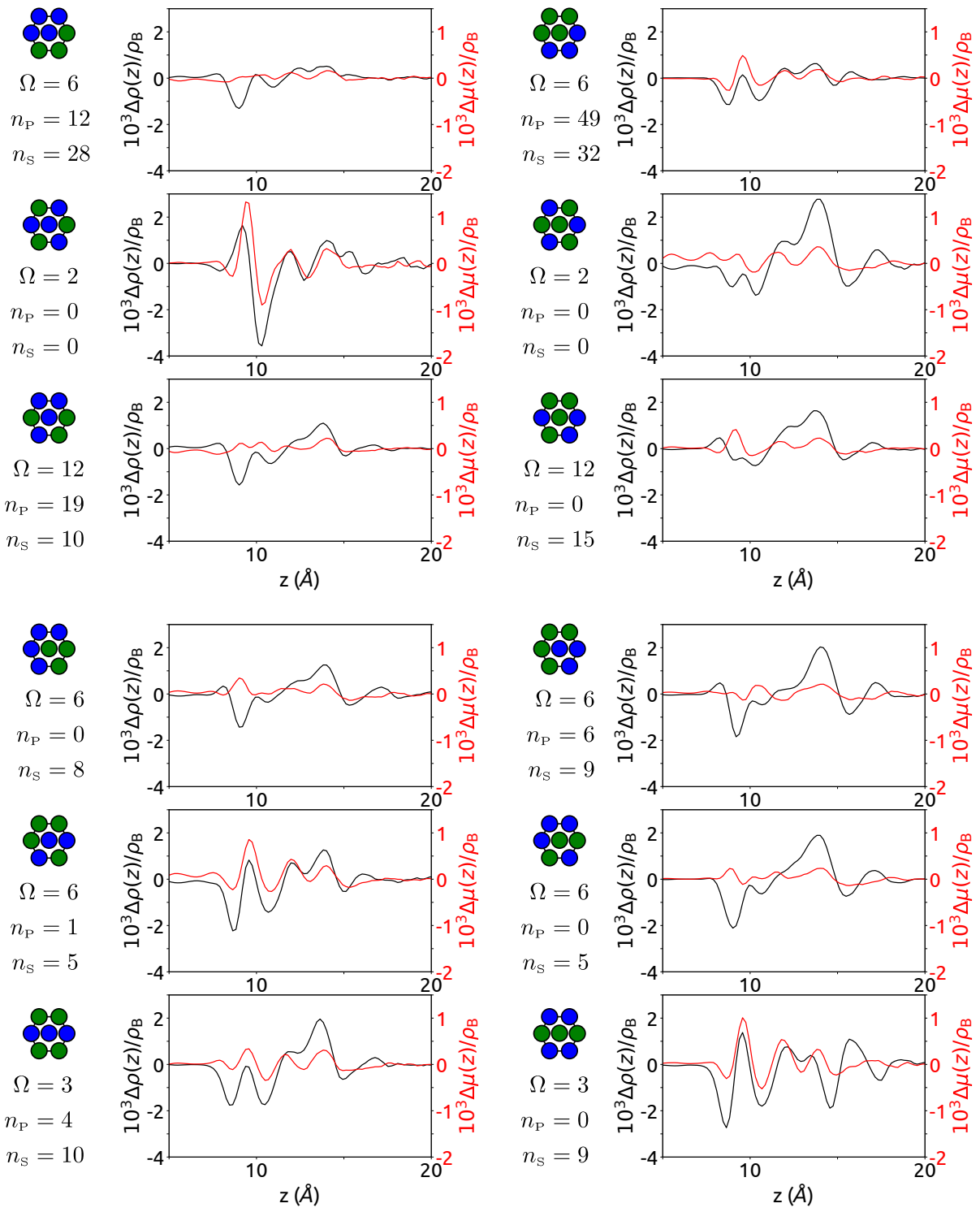

Figure S12 Excess terms associated to all the possible nearest neighbors patterns. OT and MPA ligands are shown in blue and green respectively. **Ω** stands for the degeneracy of the pattern. $\boldsymbol{n_P}$ and $\boldsymbol{n_S}$ are the number of times the pattern is observed in the patchy and stripe-like surfaces shown in figure 2D, respectively.

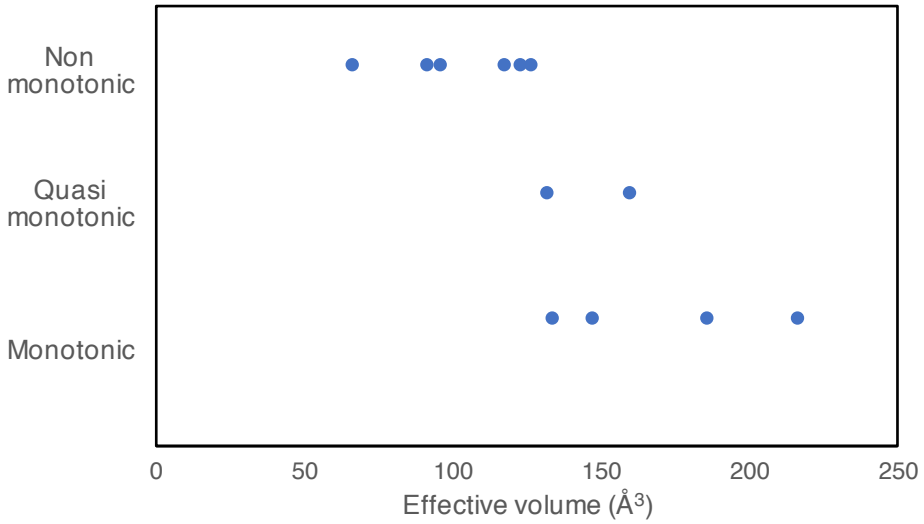

Figure S13 Re-analysis of the solubility profiles of similar MPA-OT nanoparticles as previously reported(17). The solvents are classified into three categories depending on whether the nanoparticles show monotonic dependence of solubility on ligand shell composition. The solvents are then arranged using their effective molecular volume. In general, solvents that give non-monotonic solubility behavior of the nanoparticles have smaller effective molecular volume, while solvents that give monotonic solubility behavior of the nanoparticles have larger effective molecular volume.

Table S1 Summary of the characterization on the nanoparticles.

	Patchy NP	Stripe-like NP
Core diameter	4.9 ± 0.6 nm	4.9 ± 0.6 nm
MPA: OT ratio	55%: 45%	54%: 46%
Ligand weight percentage	5.9%	5.5%
MPA domain thickness	2.1 ± 0.6 nm	1.3 ± 0.3 nm

Table S2. Values of water contact angle measured on films of NPs and corresponding work of adhesion (calculated by the Young-Dupré equation, using 72 mN/m for the surface tension of water). The error on the contact angle reported is the standard deviation of the measured values, while the error on W_{SL} is obtained by propagating the one on contact angle.

Sample	Contact Angle	Work of adhesion
Patchy Nanoparticle	76 ± 3 °	89 ± 4 mN/m
Stripe-like Nanoparticle	85 ± 3 °	79 ± 4 mN/m
MPA Nanoparticle	38 ± 1 °	128 ± 1 mN/m
OT Nanoparticle	106 ± 5 °	52 ± 6 mN/m

Table S3. Contact angle values obtained on an additional set of MPA-OT nanoparticles with ligand ratio 70:30 (as obtained by NMR) and core size 4.1 ± 0.5 nm (as obtained by TEM). These measurements confirm the fact that the wetting of the nanoparticles is affected by the shell morphology.

Sample	Contact Angle	Work of adhesion
Before annealing	72 ± 2 °	94 ± 3 mN/m
After annealing	83 ± 1 °	81 ± 1 mN/m
Difference	11 ± 1 °	13 ± 1 mN/m

Table S4. Values of surface tension (γ), density (d), molar weigth (M) and measured contact angle of various solvents on the two nanoparticle films.

Solvents	γ (mN/m)	d (g/ml)	M (g/mol)	$V_{effective}$‡ ($Å^3$)	θ_{Patchy} (°)	$\theta_{Stripe\text{-}like}$ (°)
Water(18)	72.8	1.00	18.0	30.0	70.1 ± 2.7	78.6 ± 2.9
Dichlorobenzene(18)	33.6	1.31	147.0	187.0	30.8 ± 0.8	36.1 ± 2.0
Chloroform(18)	27.5	1.49	119.4	133.0	16.6 ± 1.7	16.8 ± 2.4
Ethylene glycol(18)	47.7	1.11	62.1	92.6	52.2 ± 2.3	64.9 ± 3.3
DMSO(18)	44.0	1.10	78.1	118.0	44.7 ± 3.8	52.0 ± 3.7
Perfluorodecalin(19)	19.0	1.91	462.1	402.3	25.0 ± 1.3	27.7 ± 3.0
5CB(20)	27.9	1.00	249.4	411.0	46.3 ± 2.2	50.0 ± 1.8
Glycerol(18)	63.4	1.25	92.1	122.4	71.2 ± 4.1	87.2 ± 4.5
Hexadecane(19)	27.5	0.77	226.4	486.6	14.7 ± 2.2	25.5 ± 2.6
Isopropanol(18)	23.0	0.79	60.1	127.2	0*	6.8 ± 3.3
Formamide(21)	58.9	1.13	45.0	66.0	46.1 ± 2.0	51.6 ± 2.7
Perfluorohexane(19)	11.7	1.67	338.0	336.4	4.8 ± 1.4	5.8 ± 2.6

* $\theta = 0°$ is approximated for solvents that wet almost completely the nanoparticle film.

‡ The effective molecular volume is calculated by dividing the molar volume by Avogadro's number, i.e., $V_{effective} = \frac{M}{d*N_A}$

References

1. A. Centrone, Y. Hu, A. M. Jackson, G. Zerbi, F. Stellacci, Phase separation on mixed-monolayer-protected metal nanoparticles: A study by infrared spectroscopy and scanning tunneling microscopy. *Small* **3**, 814–817 (2007).

2. Z. Luo, *et al.*, Quantitative 3D determination of self-assembled structures on nanoparticles using small angle neutron scattering. *Nature Communications* **9**, 1343 (2018).

3. D. I. Svergun, Restoring low resolution structure of biological macromolecules from solution scattering using simulated annealing. *Biophysical journal* **76**, 2879–86 (1999).

4. D. I. Svergun, Determination of the regularization parameter in indirect-transform methods using perceptual criteria. *Journal of Applied Crystallography* **25**, 495–503 (1992).

5. P. Guyot-Sionnest, J. H. Hunt, Y. R. Shen, Sum-frequency vibrational spectroscopy of a Langmuir film: Study of molecular orientation of a two-dimensional system. *Physical Review Letters* **59**, 1597–1600 (1987).

6. O. Esenturk, R. A. Walker, Surface vibrational structure at alkane liquid/vapor interfaces. *The Journal of Chemical Physics* **125**, 174701 (2006).

7. E. Tyrode, J. Hedberg, A Comparative Study of the CD and CH Stretching Spectral Regions of Typical Surfactants Systems Using VSFS: Orientation Analysis of the Terminal CH3 and CD3 Groups. *The Journal of Physical Chemistry C* **116**, 1080–1091 (2012).

8. K. Voïtchovsky, J. J. Kuna, S. A. Contera, E. Tosatti, F. Stellacci, Direct mapping of the solid–liquid adhesion energy with subnanometre resolution. *Nature Nanotechnology* **5**, 401 (2010).

9. M. J. Abraham, *et al.*, GROMACS: High performance molecular simulations through multi-level parallelism from laptops to supercomputers. *SoftwareX* **1–2**, 19–25 (2015).

10. M. J. Robertson, J. Tirado-Rives, W. L. Jorgensen, Improved Peptide and Protein Torsional Energetics with the OPLS-AA Force Field. *Journal of Chemical Theory and Computation* **11**, 3499–3509 (2015).

11. H. J. C. Berendsen, J. R. Grigera, T. P. Straatsma, The missing term in effective pair potentials. *The Journal of Physical Chemistry* **91**, 6269–6271 (1987).

12. I. F., D. F. R., M. E., C. S., GolP: An atomistic force-field to describe the interaction of proteins with Au(111) surfaces in water. *Journal of Computational Chemistry* **30**, 1465–1476 (2008).

13. G. Bussi, D. Donadio, M. Parrinello, Canonical sampling through velocity rescaling. *J. Chem. Phys.* **126**, 014101 (2007).

14. T. Darden, D. York, L. Pedersen, Particle mesh Ewald: An N·log(N) method for Ewald sums in large systems. *The Journal of Chemical Physics* **98**, 10089–10092 (1993).

15. J. Z. Liu, A. van de Walle, G. Ghosh, M. Asta, Structure, energetics, and mechanical stability of Fe-Cu bcc alloys from first-principles calculations. *Phys. Rev. B* **72**, 144109 (2005).

16. A. Díaz-Ortiz, H. Dosch, R. Drautz, Cluster expansions in multicomponent systems: precise expansions from noisy databases. *J. Phys.: Condens. Matter* **19**, 406206 (2007).

17. A. Centrone, *et al.*, The role of nanostructure in the wetting behavior of mixed-monolayer-protected metal nanoparticles. *Proceedings of the National Academy of Sciences* **105**, 9886–9891 (2008).

18. J. Shen, *et al.*, Liquid Phase Exfoliation of Two-Dimensional Materials by Directly Probing and Matching Surface Tension Components. *Nano Letters* **15**, 5449–5454 (2015).

19. A. Luís, *et al.*, Influence of Nanosegregation on the Surface Tension of Fluorinated Ionic Liquids. *Langmuir* **32**, 6130–6139 (2016).

20. M. G. J. Gannon, T. E. Faber, The surface tension of nematic liquid crystals. *Philosophical Magazine A* **37**, 117–135 (1978).

21. B. Jańczuk, W. Wójcik, A. Zdziennicka, Determination of the components of the surface tension of some liquids from interfacial liquid-liquid tension measurements. *Journal of Colloid And Interface Science* **157**, 384–393 (1993).